

ARMY RESEARCH LABORATORY

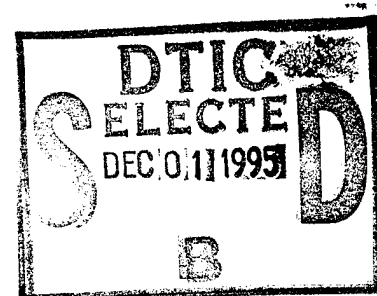


Flow Simulation and Drag Components for HEAT Projectiles With Spike and Cone Noses

Ameer G. Mikhail

ARL-TR-893

November 1995



19951130 080

APPROVED FOR PUBLIC RELEASE; DISTRIBUTION IS UNLIMITED.

DTIC QUALITY INSPECTED 5

NOTICES

Destroy this report when it is no longer needed. DO NOT return it to the originator.

Additional copies of this report may be obtained from the National Technical Information Service, U.S. Department of Commerce, 5285 Port Royal Road, Springfield, VA 22161.

The findings of this report are not to be construed as an official Department of the Army position, unless so designated by other authorized documents.

The use of trade names or manufacturers' names in this report does not constitute indorsement of any commercial product.

REPORT DOCUMENTATION PAGE			Form Approved OMB No. 0704-0188	
<small>Public reporting burden for this collection of information is estimated to average 1 hour per response, including the time for reviewing instructions, searching existing data sources, gathering and maintaining the data needed, and completing and reviewing the collection of information. Send comments regarding this burden estimate or any other aspect of this collection of information, including suggestions for reducing this burden, to Washington Headquarters Services, Directorate for Information Operations and Reports, 1215 Jefferson Davis Highway, Suite 1204, Arlington, VA 22202-4302, and to the Office of Management and Budget, Paperwork Reduction Project(0704-0188), Washington, DC 20503.</small>				
1. AGENCY USE ONLY (Leave blank)		2. REPORT DATE November 1995	3. REPORT TYPE AND DATES COVERED Final, January 1992 - January 1993	
4. TITLE AND SUBTITLE Flow Simulation and Drag Components for HEAT Projectiles with Spike and Cone Noses			5. FUNDING NUMBERS 1L162618AH80 62618A-00-00 AJ	
6. AUTHOR(S) Ameer G. Mikhail				
7. PERFORMING ORGANIZATION NAME(S) AND ADDRESS(ES) US Army Research Laboratory ATTN: AMSRL-WT-PB Aberdeen Proving Ground, MD 21005-5066			8. PERFORMING ORGANIZATION REPORT NUMBER ARL-TR-893	
9. SPONSORING/MONITORING AGENCY NAMES(S) AND ADDRESS(ES)			10. SPONSORING/MONITORING AGENCY REPORT NUMBER	
11. SUPPLEMENTARY NOTES				
12a. DISTRIBUTION/AVAILABILITY STATEMENT Approved for public release; distribution is unlimited.			12b. DISTRIBUTION CODE	
13. ABSTRACT (Maximum 200 words) Seven computations are reported for the two classes of projectile configurations of shaped charge antitank projectiles. The first class is of spiked nose with vortex generator ring, boattail, and tail fin boom. The second is of conical nose, boattail, and tail fin boom. Navier-Stokes equations are solved for the turbulent flow with dominant separation region, in an axisymmetric formulation and for zero angle of attack. Two cases at Mach numbers 3.5 and 3.0 were computed for the spiked configuration at wind tunnel Reynolds numbers. Five cases were computed for the second configuration class. Three of these cases were made at Mach numbers 4.3, 3.95, and 2.05 at sea-level conditions for the second configuration which depicts the M830A1 projectile. The other two cases were computed at wind tunnel conditions for a 40% scaled down model of an early version of the M830A1 projectile, designated as the third configuration. The flow field is computed and analyzed, providing detailed anatomy of the drag for each configuration. Comparison was made with the few body-alone wind tunnel data. This work provides details of drag components of each part of the configurations. The present work also paves the way to complete HEAT projectile viscous modeling when tail fins are included.				
14. SUBJECT TERMS aerodynamic drag, projectiles, missiles, computational fluid dynamics, supersonic flow, HEAT projectiles, spiked-nose, axisymmetric flow			15. NUMBER OF PAGES 48	
			16. PRICE CODE	
17. SECURITY CLASSIFICATION OF REPORT UNCLASSIFIED	18. SECURITY CLASSIFICATION OF THIS PAGE UNCLASSIFIED	19. SECURITY CLASSIFICATION OF ABSTRACT UNCLASSIFIED	20. LIMITATION OF ABSTRACT SAR	

INTENTIONALLY LEFT BLANK.

Table of Contents

<u>Page</u>	
List of Figures	v
I. INTRODUCTION	1
II. PROJECTILE GEOMETRIES, TEST CASES, AND TEST CONDITIONS	1
III. GOVERNING EQUATIONS	2
1. <u>Turbulence Model</u>	4
IV. THE CODE, GRIDS, AND COMPUTATIONS	4
1. <u>The Code</u>	4
2. <u>Boundary Conditions</u>	4
3. <u>Initial Conditions</u>	5
4. <u>The Grids</u>	5
a. <u>Configuration 1</u>	5
b. <u>Configurations 2 and 3</u>	6
V. RESULTS	6
1. <u>Flow Unsteadiness for Spiked Configurations</u>	6
2. <u>Configuration 1</u>	6
3. <u>Configuration 2</u>	7
4. <u>Configuration 3</u>	8
VI. SUMMARY AND CONCLUSIONS	9
References	40
List of Symbols	41

Accession For	
NTIS GRA&I	<input checked="" type="checkbox"/>
DTIC TAB	<input type="checkbox"/>
Unannounced	<input type="checkbox"/>
Justification	
By	
Distribution/	
Availability Codes	
Dist	Avail and/or Special
A-1	

INTENTIONALLY LEFT BLANK.

List of Figures

<u>Figure</u>	<u>Page</u>
1 Antitank projectile Configuration 1.	11
2 Antitank projectile Configuration 2.	12
3 Antitank projectile Configuration 3.	13
4 Computational grid: Configuration 1.	14
5 Details of the grid near the spike, Configuration 1.	15
6 Details of the grid near the boattail, Configuration 1.	16
7 Computational grid: Configuration 2.	17
8 Details of the grid near the nose tip, Configuration 2.	18
9 Details of the grid near the boattail, Configuration 2.	19
10 Computational grid: Configuration 3.	20
11 Flow-field Mach contours: Configuration 1, Mach=3.5 - Flow over the spike.	21
12 Flow-field Mach contours: Configuration 1, Mach=3.5 - Flow over the boattail.	22
13 Flow-field Mach contours: Configuration 1, Mach=3.0 - Flow over the spike.	23
14 Flow-field Mach contours: Configuration 1, Mach=3.0 - Flow over the boattail.	24
15 Flow-field Mach contours: Configuration 2, Mach=4.3 - Flow near the nose.	25
16 Flow-field Mach contours: Configuration 2, Mach=4.3 - Flow near the shoulder.	26
17 Flow-field Mach contours: Configuration 2, Mach=4.3 - Flow near the boattail.	27
18 Flow-field Mach contours: Configuration 2, Mach=2.05 - Flow near the nose.	28
19 Flow-field Mach contours: Configuration 2, Mach=2.05 - Flow near the shoulder.	29
20 Flow-field Mach contours: Configuration 2, Mach=2.05 - Flow over the boattail.	30
21 Total forebody drag coefficient for Config. 1.	31
22 Surface pressure distribution for Config. 1, at M=3.5.	32
23 Drag coefficient composition for Config. 1, at M=3.0.	33
24 Total forebody drag coefficient for Config. 2.	34
25 Surface pressure distribution for Config. 2, at M=2.05.	35
26 Drag coefficient composition for Config. 2, at M=4.3.	36
27 Total forebody drag coefficient for Config. 3.	37

28	Surface pressure distribution for Config. 3, at $M=3.5$	38
29	Drag coefficient composition for Config. 3, at $M=3.5$ and 3.0.	39

I. INTRODUCTION

Spike-nosed projectile configurations, Fig. 1, are fired at armored targets where the spike provides a standoff distance between the armor and the shaped charge warhead of the projectile. However, the cone-nosed configurations, Figs. 2 and 3, provide a windshield to reduce the drag and provide a standoff distance as well. The hoped for lower drag for these projectiles should extend their range, if the projectiles are launched at the same speed. This cone-nosed configuration can then be used against semi-hardened or "soft" targets, such as helicopters, at greater distances. Thus, the name "multi-purpose" is used instead of "antitank" projectile. A survey of the prior art regarding spiked bodies was made and is listed in the earlier work of Refs. 1 and 2.

In prior studies^{1, 2}, Mikhail presented computational results for spiked configurations with increasing geometrical complexity. In Ref. 1, configurations of spikes with no vortex rings and bodies with no base flow simulations were considered. In Ref. 2, the vortex generator ring was added and the body base flow was computed. In the present work, an aftbody with steep boattail and tail fin boom is added. The present work lays the foundation for the next and final step, which is to include fins on the boom.

The computations were made using the axisymmetric flow simulation code using zonal overlapping grid of Ref. 3. It uses the explicit, time-dependent, McCormack's robust numerical scheme. The purpose of this work is to provide the drag information of every geometrical component of the projectile body without fins, for both the spike- and the cone-nosed projectiles, at high supersonic speeds and zero angle of attack. The specific configurations considered and the test cases with their conditions are provided next.

II. PROJECTILE GEOMETRIES, TEST CASES, AND TEST CONDITIONS

Before computing a real projectile with fins, the logical step was to test the computation on a simpler configurations with the tail boom but without the fins. Experimental data were sought before the computations were performed. The computations need to be assessed and validated before they can be claimed successful and reliable. Only wind tunnel data were expected to exist, since without fins, these projectiles are statically unstable and therefore unsuitable for range tests.

Two sets of wind tunnel data were located. The first set⁴ is for transonic ($0.9 \leq M \leq 1.1$) and low supersonic ($M=1.2$ and 1.4) speeds. They were for a 3.543-inch (90-mm) shoulder-fired, antitank, spiked projectile for a recoilless launcher. Unfortunately, no tests were made at the high supersonic speeds ($M = 3.0 - 4.5$), which is of interest to the present work. This configuration is named Config. 1 in this study.

Successful computations were made at Mach =3.5 and 3.0. Attempts were made for computing the cases at Mach 1.2 and 1.4 but yielded very large, unperiodic flow oscillations which were not indicated in Ref. 4. However, small oscillations were reported for a similar projectile in Ref. 5. Thus, these two lower Mach number cases could not be used for

validation. The tests were made at the NASA 2-ft continuous flow transonic wind tunnel for the full-scale model. The wind tunnel conditions for the $M=1.2$ and 1.4 cases were 14.85 psi (102.4 kPa) for the total pressure and 6.29 psi (43.4 kPa) for the dynamic pressure. The unit Reynolds number was 4.5×10^6 per foot (14.76×10^6 per meter).

The second projectile configuration (Config. 2) is the 120-mm M830A1 multi-purpose sub-caliber projectile with the tail fin boom but without the fins. The body diameter is 3.124 inch (80 mm). It has a bi-boattail with slopes of 12.5° and 4.5° . Computations were made at $M = 4.30, 3.95$, and 2.05 . These speeds were chosen because the actual projectile (with fins) was fired at the U.S. Army Research Laboratory (ARL) range, and data exist for them at these Mach numbers. However, as mentioned before, no range firings were made for the unstable, no-fin configuration. It was thought that in future computational efforts, when the fins are added, the present computations would be the starting point for comparison with the data. The range conditions are sea-level conditions of $p=14.7$ psi (101.3 kPa) and $T=60^\circ F$ ($15.5C$). The unit Reynolds numbers were 30.1, 27.6, and 14.3×10^6 /ft (98.7, 90.55, and 46.9×10^6 /m) for $M=4.3, 3.95$, and 2.05 , respectively. With no positive validation available for this configuration, a similar configuration (Config. 3) that has data was chosen next for computation and comparison.

The third and last configuration (Config. 3) is a 40% scaled down model of an earlier version of the M830A1 projectile. Wind tunnel test results were available in the second data reference⁶ mentioned earlier. The tests were made in a 9-inch (22.5-cm) blow-down supersonic wind tunnel at $M = 3.5$ and 3.0 . The model had a diameter of 1.261 inch (32 mm) and a bi-boattail with slopes of 20.5° and 4.6° . The tunnel total pressure was 75 and 60 psi, respectively (517.2 and 413.8 kPa). The total temperature was $60F^\circ$ ($17.5C$). The unit Reynolds number was 9.1 and 10.2×10^6 /ft (29.9 and 33.5×10^6 /m). No error bounds were given for these measurements. However, calibrations errors of the tunnel balance were mentioned as possible error source.

III. GOVERNING EQUATIONS

The compressible Navier-Stokes equations for axisymmetric and two-dimensional flow can be expressed^{1, 2, 3} in the following strong conservation form in which the dependent variables ρ, u, v , and e are mass averaged, in which e is the specific total energy, T is the temperature, ρ and p are the mean density and pressure, respectively, and t is time:

$$\frac{\partial Q'}{\partial t} + \frac{\partial E'}{\partial x} + \frac{\partial F'}{\partial y} + \left(\frac{F'}{y} + \frac{H'}{y} \right) \beta = 0$$

in which

$$Q' = \begin{bmatrix} \rho \\ \rho u \\ \rho v \\ \rho e \end{bmatrix} \quad E' = \begin{bmatrix} \rho u \\ \rho u u + p - \tau_{xx} \\ \rho u v - \tau_{xy} \\ (\rho e + p)u - \tau_{xx}u - \tau_{xy}v + \dot{q}_x \end{bmatrix}$$

$$F' = \begin{bmatrix} \rho v \\ \rho uv - \tau_{xy} \\ \rho vv + p - \tau_{yy} \\ (\rho e + p)v - \tau_{xy}u - \tau_{yy}v + \dot{q}_y \end{bmatrix}$$

$$H' = \begin{bmatrix} 0 \\ 0 \\ -p + \sigma_+ \\ 0 \end{bmatrix}$$

$$\tau_{xx} = -\frac{2}{3}(\mu + \epsilon)\tilde{\nabla} \times \tilde{V} + 2(\mu + \epsilon)\frac{\partial u}{\partial x}$$

$$\tau_{xy} = (\mu + \epsilon)\left(\frac{\partial u}{\partial y} + \frac{\partial v}{\partial x}\right) \quad (1)$$

$$\tau_{yy} = -\frac{2}{3}(\mu + \epsilon)\tilde{\nabla} \times \tilde{V} + 2(\mu + \epsilon)\frac{\partial v}{\partial y}$$

$$\tau_{\Theta\Theta} = \sigma_+ = -\frac{2}{3}(\mu + \epsilon)\tilde{\nabla} \times \tilde{V} + 2(\mu + \epsilon)\frac{v}{y}$$

$$\tilde{\nabla} \times \tilde{V} = \frac{\partial u}{\partial x} + \frac{\partial v}{\partial y} = \left(\frac{v}{y}\right)\beta$$

$$\dot{q}_x = -C_p\left(\frac{\mu}{Pr} + \frac{\epsilon}{Pr_t}\right)\frac{\partial T}{\partial x}$$

$$\dot{q}_y = -C_p\left(\frac{\mu}{Pr} + \frac{\epsilon}{Pr_t}\right)\frac{\partial T}{\partial y}$$

in which μ is the molecular viscosity, ϵ is eddy viscosity and $\beta = 1$ or 0 for axisymmetric or two-dimensional cases, respectively.

The air is assumed to be a perfect gas. Sutherland's law for temperature dependence of the laminar viscosity was used.

The laminar and turbulent Prandtl numbers, Pr and Pr_t , were assumed constant with values of 0.72 and 0.9 , respectively. The ratio of the specific heats, γ , was also assumed

constant and equal to 1.4. C_v and C_p are the specific heat capacities at constant volume and constant pressure, respectively.

The total energy per unit mass, e , is given by

$$e = C_v T + (1/2)(u^2 + v^2).$$

In the $\xi - \eta$ computational plane, Equation 1 is transformed to the conservation law form and the equations can be found, for example, in Ref. 3.

1. **Turbulence Model** Turbulence is modeled through a modification of the eddy viscosity model of Baldwin and Lomax⁷. This widely applied model employs the two-layer concept (inner and outer layers).

Because of the perpendicular surfaces of the spike surfaces at the nose tip and at the facing shoulder, the normal distance to the wall " y " in the turbulence model is difficult to assign⁸. This problem was approached in Ref. 8 by measuring y along a 45° ray emanating from the point of intersection of the two perpendicular walls.

IV. THE CODE, GRIDS, AND COMPUTATIONS

1. **The Code** The computer code was developed by Patel et al.³ and uses the robust explicit, time-dependent method of McCormack. Explicit schemes must run with small, limited time step sizes and are often slow in comparison with implicit schemes. However, for the present study, robustness was favored over computer time economization, a matter left for possible future efforts. The code is vectorized and is run on a Cray-XMP/48 machine. However, the present computations were all run in serial arithmetic mode to avoid uncertainties in parallelization. The zonal grid and overlapping is provided in the code and is represented by eight different available zones, which may be increased if desired. A global uniform time step was used herein against grid-varying time steps to simulate "time-accurate" solutions and to avoid introduction of numerical unsteadiness that may interfere with possible physical flow unsteadiness. The time step is determined from the CFL (Courant-Fredrich-Levy) condition, with a conservative factor of 0.6 being used as the Courant number to avoid any instabilities that may be triggered by physical or numerical unsteadiness. The computation takes 0.7×10^{-5} sec per one time step. This amounts to about 1950 and 1150 CPU seconds per grid point per one thousand time steps for the larger grid of Config. 1 and the smaller grid of both Configs. 2 and 3, respectively.

2. **Boundary Conditions** No-slip conditions are specified on all wall surfaces. The incoming flow conditions are assumed to be of uniform profiles with free-stream values based on the wind tunnel test conditions or sea level as given in Section II. The out-going flow conditions at the downstream end of the flow field were imposed as zero gradients at the body tail boom end plane.

The outer boundary conditions were imposed as nonreflective conditions, i.e., zero gradient conditions along characteristic lines for all variables. The characteristic direction is determined from the local velocity and temperature. This approach allows setting the "outer" field close to the body without the penalty of any unnecessary approximation regarding shock reflection at the boundary or any degradation attributable to the far-field conditions (zero-gradients) being set too close.

At the symmetry line, ahead of the spike tip, a two-point zero gradient boundary condition is imposed on the solved variables.

3. Initial Conditions For Configuration 1, the $M=3.5$ case was computed first. The computations started with uniform, free-stream condition values for all the variables. The $M=3.0$ case was then started using partially converged solution of the $M=3.5$ case.

For Config. 2, the $M=4.3$ case was computed first using all free-stream flow conditions as starting flow field. The cases of $M=3.95$ and 2.05 were then started using partially converged solution of the $M=4.3$ case.

For Config. 3, the same was done by starting the case of $M=3.5$ with uniform flow fields, then the case of $M=3.0$ was initiated using the obtained converged solution of the $M=3.5$ case.

4. The Grids

a. Configuration 1 Five overlapping zones were used in the computations. Originally, the zones had the grids of (20×89) , (17×72) , (11×65) , (70×88) , and $(130, 36)$, respectively. The first and second arguments in the parentheses refer to the axial and radial directions, respectively. This grid is equivalent to 14,559 total points or an equivalent (121×121) grid. Computations at $M=3.0$ and 3.5 yielded very large, nonperiodic oscillations and did not converge. The grid was then almost doubled to 28,000 points distributed as (35×131) , (17×114) , (11×107) , (105×124) , and (130×56) . This grid is equivalent to (168×168) mesh. The solution convergence instability was then controlled, leaving only the smaller, physical oscillations attributable to the vortex break-up. The Mach 3.5 and 3.0 cases were computed. However, the lower Mach number cases of 1.2 and 1.4 still did not converge. This numerical behavior for the lower Mach numbers is believed to be physical in nature, as described by the unsteady flow patterns described and captured in shadowgraphs by Biele⁵. Success in obtaining solutions for the $M=3.5$ and 3.0 cases indicates that these oscillations at $M = 1.2$ and 1.4 are not to be considered as numerical in nature or attributable to coarse grid. Further investigation should be pursued to resolve this issue.

The radial grid is exponentially distributed. The first point distance to the wall, Δy_1 is used as an input for possible grid-spacing variation. Figures 4, 5, and 6 show the grid for this configuration.

b. **Configurations 2 and 3** Both configurations were computed using five-zone overlapping grids. The total grid number was 15,837 points, equivalent to a (126x126) mesh. The grid was distributed as (25x69), (31x56), (32x56), (80x56), and (109x56). The effect of the size of Δy_1 was tested and is given in the results section. The grid is shown in Figs. 7, 8, and 9 for Configuration 2; and Fig. 10 for Configuration 3.

V. RESULTS

1. **Flow Unsteadiness for Spiked Configurations** The work of Haupt et al.⁹ for range shadowgraph studies at transonic speeds of $M = 0.75$ to 1.24 , has documented large scale flow oscillations for both the low and high drag modes. These oscillations, similar to what Mikhail computationally reported² for the $M=1.9$ case, are attributable to the break-up and re-generation of vortices in the highly separated flow on the spike, behind the vortex generator ring. These oscillations are different from those occurring when the flow transitions between the high and low drag modes. This latter type of oscillation was reported and studied by Calarese¹⁰ and Shang¹¹ for a re-entry vehicle with a short spike. The former oscillations for a high or low drag case were encountered in the present work when the Mach number was lowered to $M=1.9$, 1.4 , and 1.2 . Very large flow oscillations continued in the computations and no steady flow pattern was observed. Biele⁵, also using firing range shadowgraphs for spiked projectiles for Mach 0.9 - 3.5 , indicated that the flow was unsteady because of vortex shedding from the vortex ring at Mach 1.4 and 2.6 . However, the same projectile was also reported to have no flow unsteadiness when fired at either Mach 3.1 or 1.85 . Biele indicates that there are at least three different flow patterns which the projectile goes through when decelerating from $M=3.1$ to 1.2 . He explains that the drag/Mach number curve shows waviness because of this phenomenon of the combination of those three flow patterns. Spike length, spike-to-body diameter ratio, flow Reynolds and Mach numbers are the main parameters influencing the occurrence of these patterns.

2. **Configuration 1** Computations were made for the $M = 3.5$ and 3.0 cases using a wall-dense grid distribution with Δy_1 of 1×10^{-4} inch (2.5×10^{-3} mm). The flow exhibited constant flow oscillations because of the break-up of vortices. The areas distinctly affected by the flow oscillations are the tip of the spike and the boattail regions. The flow was unsteady but close to being periodic. The same flow unsteadiness was also reported² for a similar spike-nosed body. Because the code and scheme were validated earlier^{1,2} for similar spiked configuration, the present computations were considered satisfactory, being an additional application for this class of projectiles.

The flow field, represented by the Mach contours, for the $M=3.5$ case is shown near the spike and the boattail regions in Figs. 11 and 12. Noted is the vortex sheet (surface) emanating from the vortex ring to the body shoulder, then over the tail boom. Noted also, as was reported earlier by Mikhail², is that this sheet does not "bend" down to follow the boattail. Thus, no Mach expansion fan is observed at the body-boattail junction, as evidenced from Fig. 12. The flow at the spike tip pulsed with the small eddy break-up cycle. The bow shock changed shapes from normal to the body axis to a sloped shock. Figure 11 shows the sloped form. The second case at $M=3.0$ gave very similar results. Figures 13

and 14 depict the same flow field pattern near the spike and the boattail regions for that case.

The total forebody drag coefficient (total drag minus the tail boom base drag) was 0.256 at $M=3.0$ and decreased to 0.245 at $M=3.5$, as given in Fig. 21. Figure 22 depicts the surface pressure distribution for $M=3.5$, while Fig. 23 presents the configuration with its component drag for $M=3.0$. The case of $M=3.5$, not surprisingly, gave similar drag anatomy. The drag anatomy for the two cases is listed in Table 1.

Table 1. Drag Anatomy for Configuration 1

<i>Drag Component</i>	$M = 3.5$		$M = 3.0$	
	<i>Cd</i>	<i>Cd %</i>	<i>Cd</i>	<i>Cd %</i>
<i>Spike Tip Face</i>	0.0739	30.16	0.0641	25.03
<i>Vortex Ring (both sides)</i>	0.0068	2.78	0.0055	2.16
<i>Main Shoulder Face</i>	0.1391	56.79	0.1545	60.36
<i>Boattail</i>	0.0250	10.23	0.0312	12.19
<i>Viscous Drag (all body)</i>	0.0006	0.24	0.0007	0.26
<i>Total Drag</i>	0.2454	100.00	0.2560	100.00

Finally, it is very interesting to observe the very low viscous drag percentage for the configuration. One is reminded that the flow is separated over the spike, the boattail, and most of the tail boom. Therefore, only the main body diameter and part of the tail boom, with its small surface area, contribute positively to the viscous drag.

3. Configuration 2 Three Mach cases of 4.3, 3.95, and 2.05 were computed using the grid described in Section IV-4b. Two grid spacings were tested to indicate the viscous flow resolution near the body surface. The first grid spacing used Δy_1 of 0.005 inch (0.127 mm), as very coarse distribution. The second was very fine and fifty times smaller, having Δy_1 of 0.0001 inch (0.0025 mm). Obviously, for the present explicit numerical scheme, a larger computer time (fifty times larger) will be needed because of the smaller time step value that will be used. This test was made to check the effect of grid spacing and resolution on the drag values.

Usually, numerical convergence becomes much slower near transonic and low supersonic speeds. Also, separated flow regions, such as base flow or the boattail flow in the present case, usually take the longest time to converge, while the forebody flow field reaches its steady state relatively quickly. The present cases are no exception. The $M = 4.3$ and 3.95 cases converged quickly for both grid resolutions, while the 2.05 case was significantly slower to converge. The fine spacing gave no improvements for the total drag for the $M=4.3$ and 3.95 cases. Some 4% increase in the total drag (basically from the separated boattail region)

was observed for the $M=2.05$ case. However, the viscous drag changed very little. This improvement should be balanced by such large increase in required computing time.

The Mach contours for the $M=4.3$ case are shown in Figs. 15, 16, and 17. Figure 17 shows how the flow follows the body contour in the boattail region, causing the expected Mach expansion fan unlike in Config. 1 case. The case of $M=2.05$ is also shown in Figs. 18, 19, and 20, with no major differences in the flow pattern. The total forebody drag for the three cases was 0.2984, 0.1905, and 0.1796 for $M=2.05$, 3.95 and 4.3, respectively, as also given in Fig. 24. The groove drag was computed using the correlation of Ref. 12 and is included in the given values.

The drag anatomy for the $M=4.3$ case is listed below, together with the other two Mach numbers. The viscous drag is very small in this case because of the very high Reynolds number, which was 30.1×10^6 /ft (98.2×10^6 /m). This viscous drag value will triple when the Reynolds number decreases as will be shown in the case of Config. 3. The groove drag for $M=2.05$ is slightly high since it is outside the Mach speed range of Ref. 12. The surface pressure distribution for $M=2.05$ and the components drag for $M=4.3$ are shown in Figs. 25 and 26, respectively. They are also listed in Table 2.

Table 2. Drag Anatomy for Configuration 2

Drag Component	$M = 4.3$		$M = 3.95$		$M = 2.05$	
	C_d	$C_d \%$	C_d	$C_d \%$	C_d	$C_d \%$
<i>Tip Meplat Face</i>	0.0136	7.60	0.0138	7.25	0.0129	4.31
<i>Nose</i>	0.1151	64.10	0.1177	61.79	0.1528	51.19
<i>Boattails</i>	0.0447	24.90	0.0519	27.25	0.1105	37.05
<i>Viscous Drag (all body)</i>	0.0047	2.61	0.0053	2.76	0.0098	3.29
<i>Groove Drag</i>	0.0014	0.79	0.0018	0.95	0.0124	4.16
<i>Total Drag</i>	0.1796	100.00	0.1905	100.00	0.2984	100.00

Since the computations were not validated against experiment for this type of configuration, the following case of Config. 3, which is very similar and has experimental data, was then computed for validation.

4. Configuration 3 This 40% scaled down model was computed using the dense grid spacing of Δy_1 of 0.0001 inch (0.0025 mm) and the same number of grid points as Config. 2. The two cases of Mach 3.5 and 3.0 were computed without difficulty and without any unsteadiness in the flow. The computed total drag coefficient was 0.2668 compared to the measured value of 0.253 of Ref. 4. For the $M=3.5$ case, the computed value was 0.2387 compared to 0.257 for the wind tunnel. This last wind tunnel value is considered slightly in error since it shows value greater than the $M=3.0$ case, as shown in Fig. 27. Usually,

the drag coefficient decreases with the Mach number rather than increases. The present computation conforms and yields the correct trend.

The drag composition for the two cases is listed in Table 3. The surface pressure is given in Fig. 28 for $M=3.5$ case. The case of $M=3.0$ gave a similar drag composition and is depicted with $M=3.5$ case in Fig. 29.

Table 3. Drag Anatomy for Configuration 3

<i>Drag Component</i>	<i>M = 3.5</i>		<i>M = 3.0</i>	
	<i>Cd</i>	<i>Cd %</i>	<i>Cd</i>	<i>Cd %</i>
<i>Tip Meplat Face</i>	0.0045	1.90	0.0047	1.75
<i>Nose</i>	0.1434	60.06	0.1512	56.67
<i>Boattails</i>	0.0657	27.52	0.0843	31.60
<i>Viscous Drag (all body)</i>	0.0197	8.25	0.0194	7.27
<i>Groove Drag</i>	0.0054	2.27	0.0072	2.71
<i>Total Drag</i>	0.2387	100.00	0.2668	100.00

Notice that the viscous drag has increased to 8.2% because of the lower Reynolds number compared to the high Reynolds number case of Config. 2. Also, the meplat drag is smaller than in Config. 2 due to a smaller meplat.

The overall computations are believed to be validated and acceptable. Therefore, the above cases of Config. 2, which is very similar in shape, are considered satisfactorily computed.

VI. SUMMARY AND CONCLUSIONS

Seven different cases were computed for three projectile configurations encompassing the two categories of anti-ank projectiles. Computations were made at both wind tunnel and sea-level Reynolds numbers. The results obtained are summarized as follows:

1. The flow over a spike-nosed configuration (Config. 1) with vortex generator ring, boattail, and tail fin boom was computed at Mach 3.5 and 3.0 at a wind tunnel Reynolds number of $4.5 \times 10^6/\text{ft}$ and zero angle of attack. The computed spike flow features were consistent with the prior computations and validation of Ref. (2). The new boattail and fin boom flow indicated that the vortex sheet (surface) extended over the boattail, thus inhibiting the usual wave expansion fan expected at the body-boattail junction. The flow exhibited a small unsteadiness pattern near the spike tip, probably triggered by the subsonic region at that location.

Flow oscillation on the spike is an undesirable factor because it may interact with the yawing motion of the projectile and thus, may become amplified itself or may rather increase the yawing motion, rendering the projectile unstable or causing large dispersion.

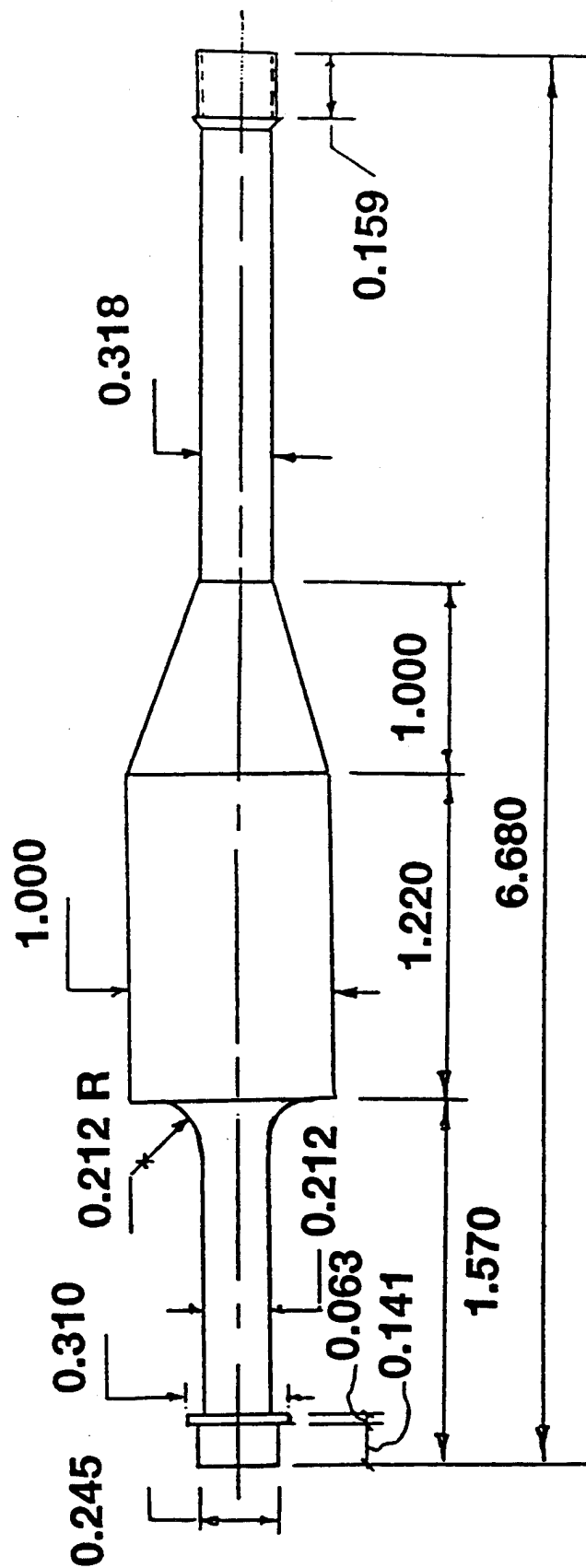
2. The flow over the cone-nosed body of the M830A1 projectile with the 12.5° and 4.5° bi-boattails (Config. 2) was computed for Mach 4.3, 3.95, and 2.05 at sea-level Reynolds numbers of 30.1, 27.6, and $14.3 \times 10^6/\text{ft}$, respectively. The flow showed very small flow unsteadiness at the nose meplat at Mach 4.3, but it disappeared at Mach 2.05. There were evident expansion waves at the body-boattail junction because of the absence of the vortex sheet of the vortex ring of the spiked configuration.

3. The 40% scaled down model, cone-nosed configuration of 20.5° and 4.6° bi-boattails (Config. 3) was computed at wind tunnel Reynolds numbers of 9.1 and $10.2 \times 10^6/\text{ft}$ for Mach 3.5 and 3.0, respectively. The axial force coefficient was compared with data and indicated a measurement error at Mach 3.5 where the value increased rather than decreased, differently than the normal trend.

4. Drag component anatomy was made for all cases computed. For the spiked cases, the spike tip and body shoulder contributed 25% and 60% of the total drag at $M=3$. For the coned configuration (Config. 3), the nose contributed 57% while the boattails added 32%, respectively, at Mach 3. This insight of the drag components is a significant contribution of the present work. No experiment has, yet, provided such an insight.

5. Contrary to the general expectation, the spike-nosed configuration drag was not much higher than the cone-nosed drag in the Mach 3.0-to-3.5 range. This finding is limited to spiked bodies with vortex generator rings, at the low-drag mode, at $M \geq 3.0$. A spiked body without the ring can suffer much higher drag than cone-nosed body at lower speeds ($M < 3$), especially at the spike high drag mode.

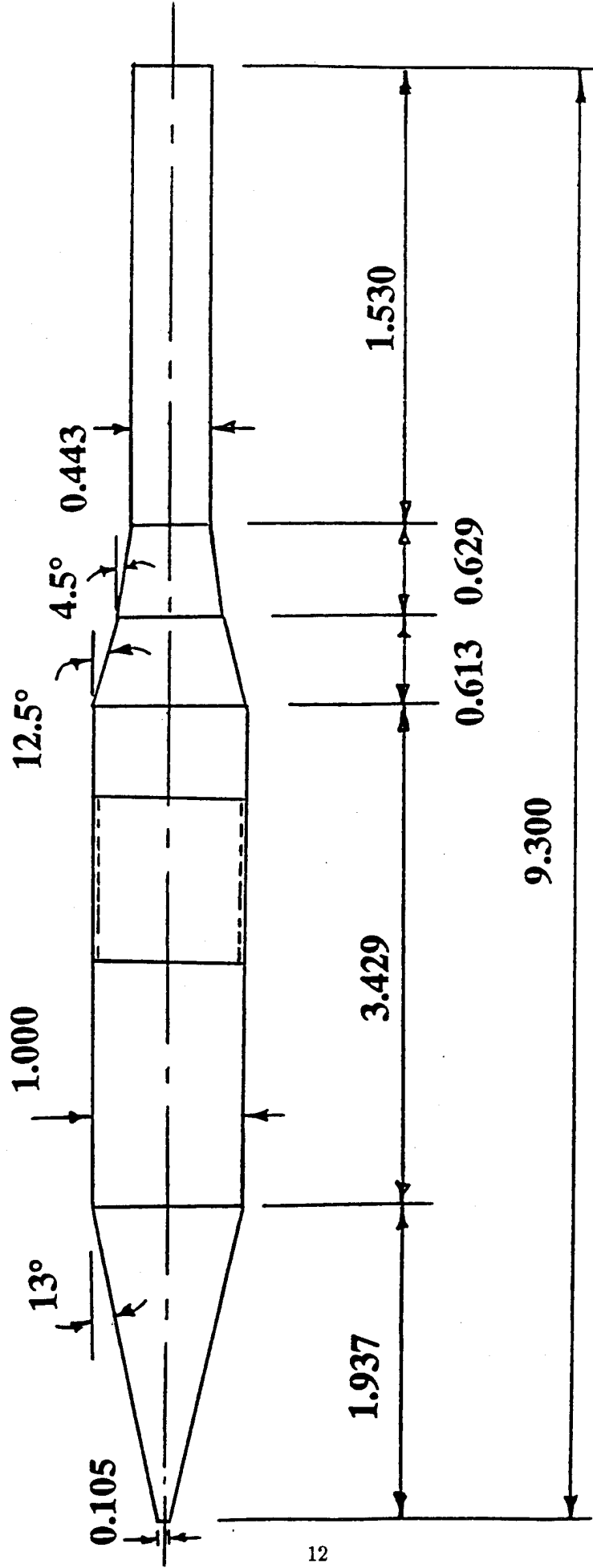
6. The present computations indicated that these two classes of configurations can be successfully computed with the presented approach. This work, therefore, paves the way to computing the complete HEAT projectile configuration by including the fins.



DIMENSIONS IN CALIBERS
One Caliber = 90 mm = 3.543 inches

CONFIGURATION 1

Figure 1. Antitank projectile Configuration 1.

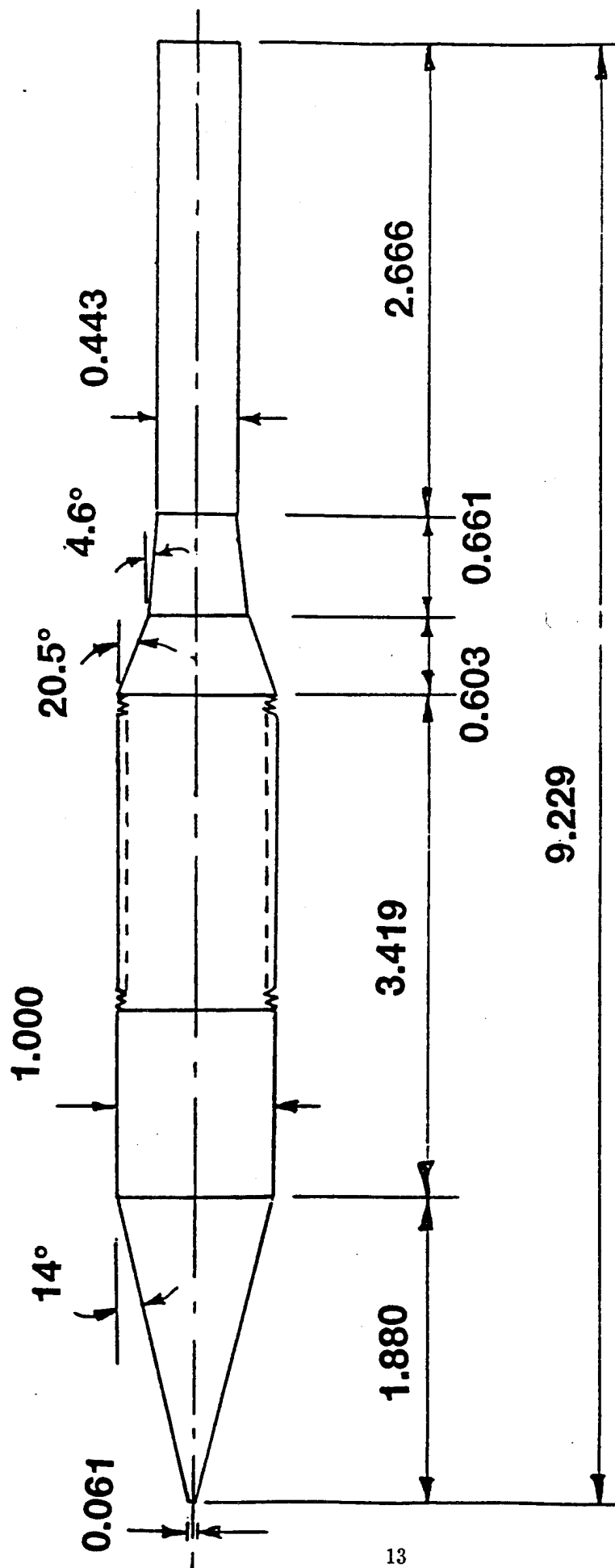


DIMENSIONS IN CALIBERS

One Caliber = 32 mm = 1.261 inches

CONFIGURATION 2

Figure 2. Antitank projectile Configuration 2.



DIMENSIONS IN CALIBERS
One Caliber = 32 mm = 1.261 inches

CONFIGURATION 3

Figure 3. Antitank projectile Configuration 3.

GRID

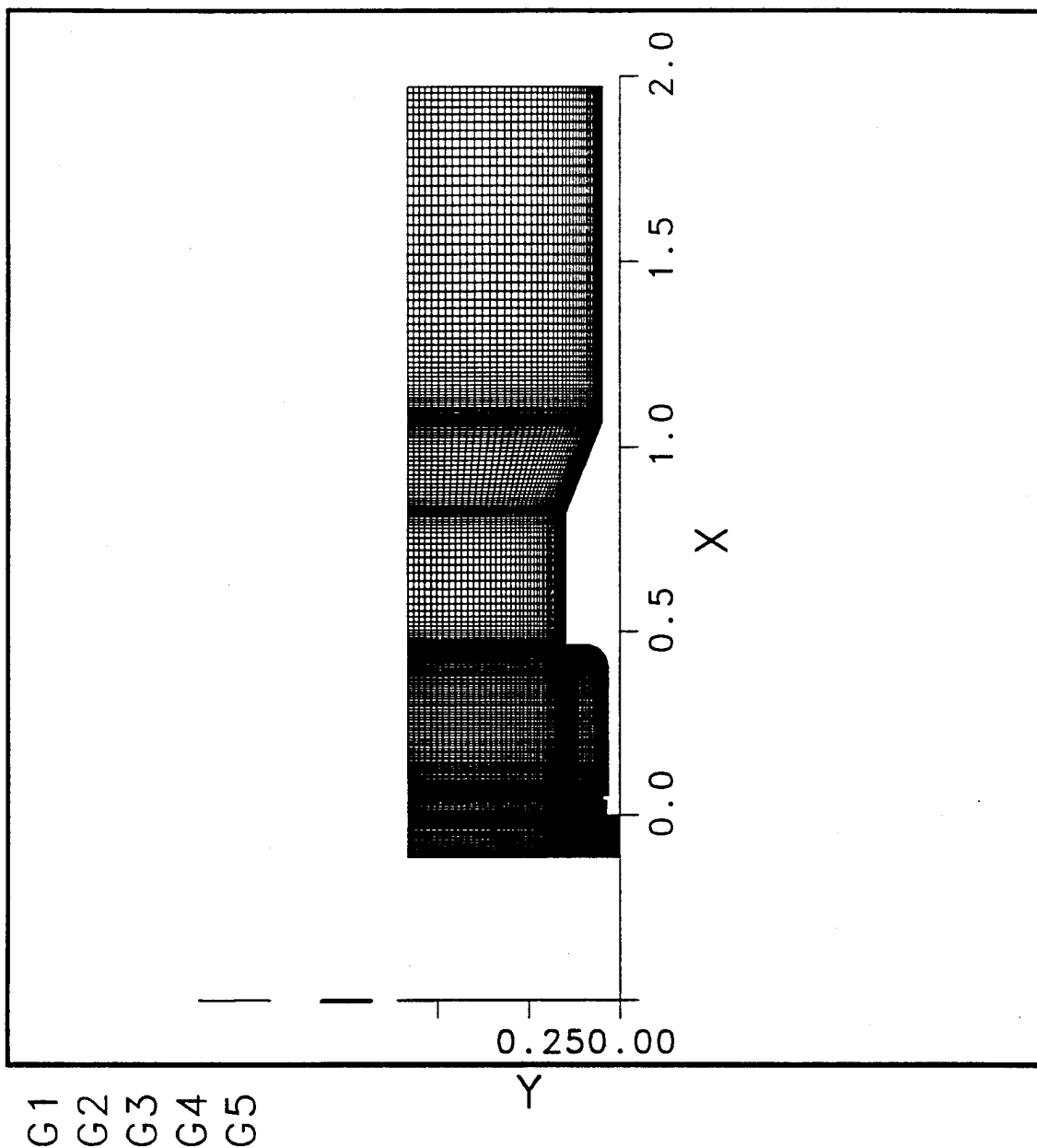


Figure 4. Computational grid: Configuration 1.

GRID

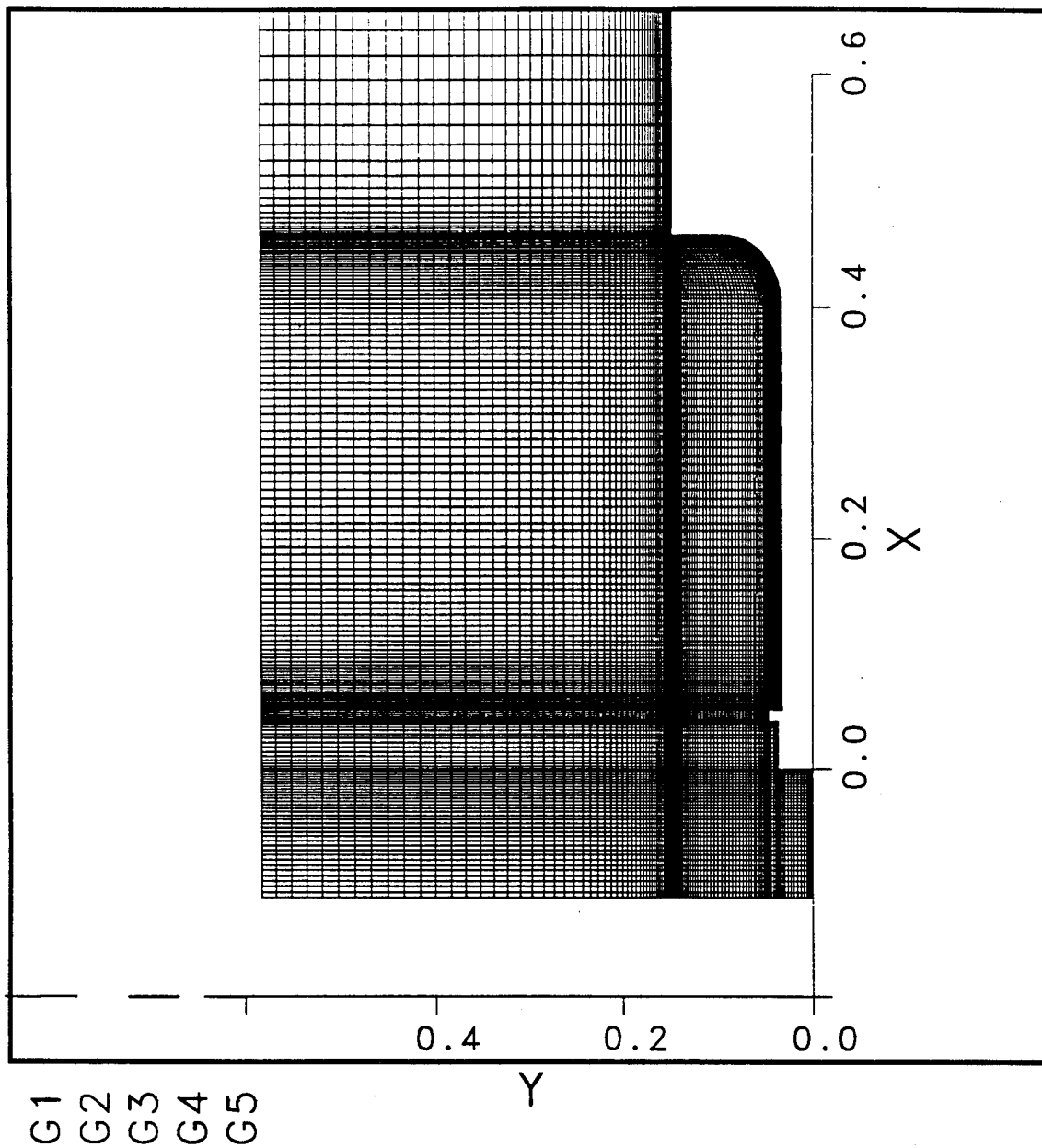


Figure 5. Details of the grid near the spike, Configuration 1.

GRID

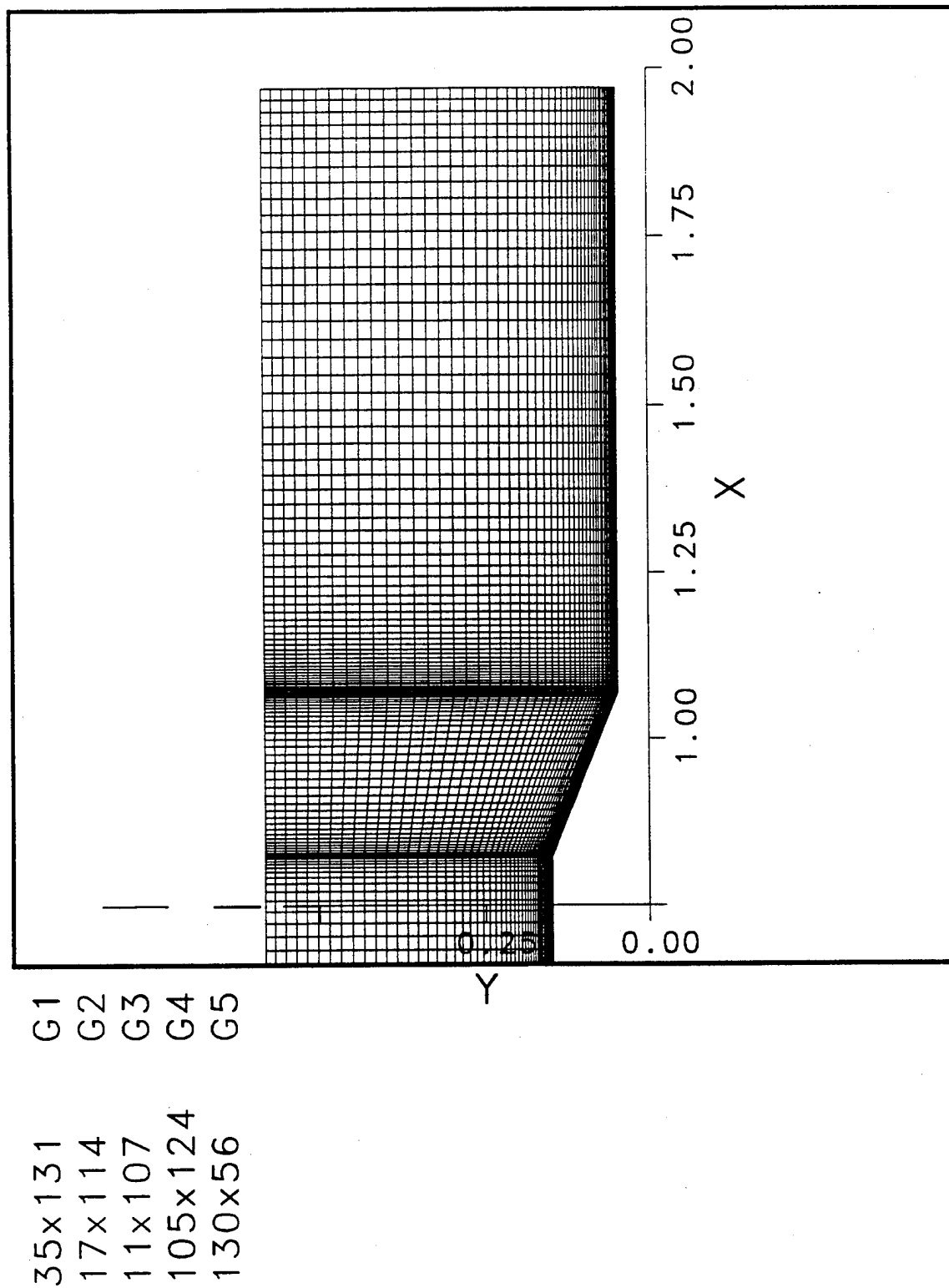


Figure 6. Details of the grid near the boattail, Configuration 1.

GRID

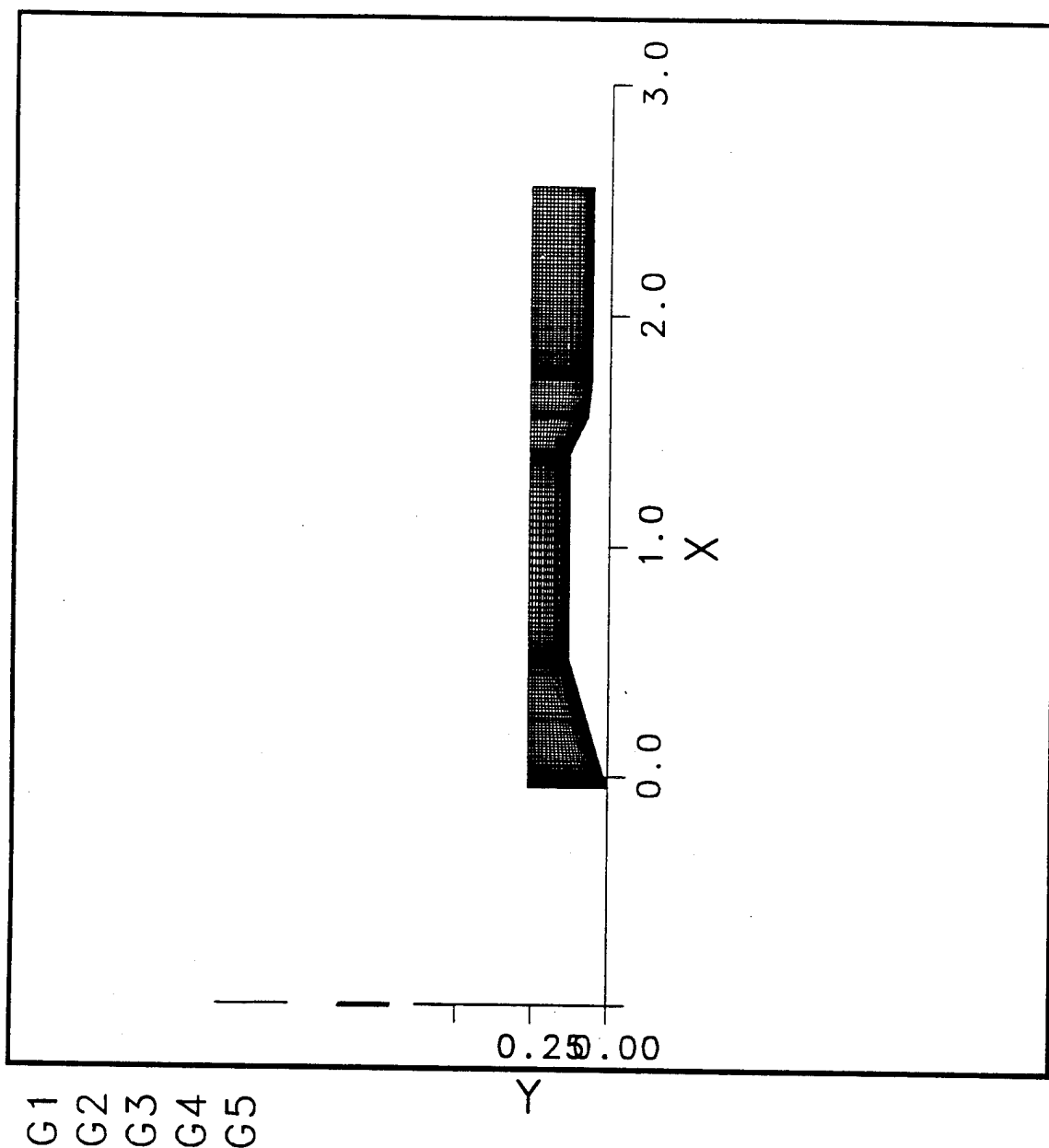


Figure 7. Computational grid: Configuration 2.

GRID

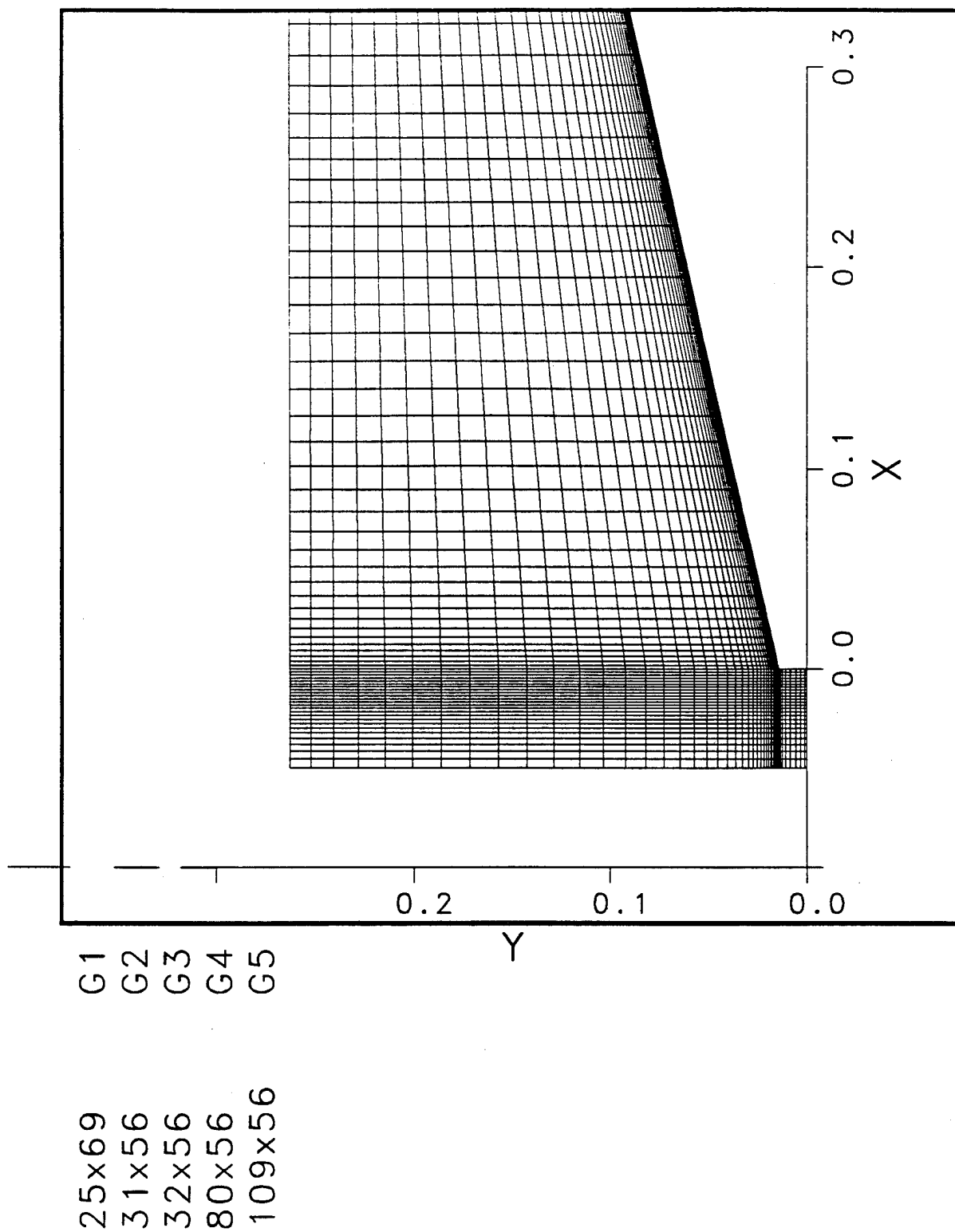


Figure 8. Details of the grid near the nose tip, Configuration 2.

GRID

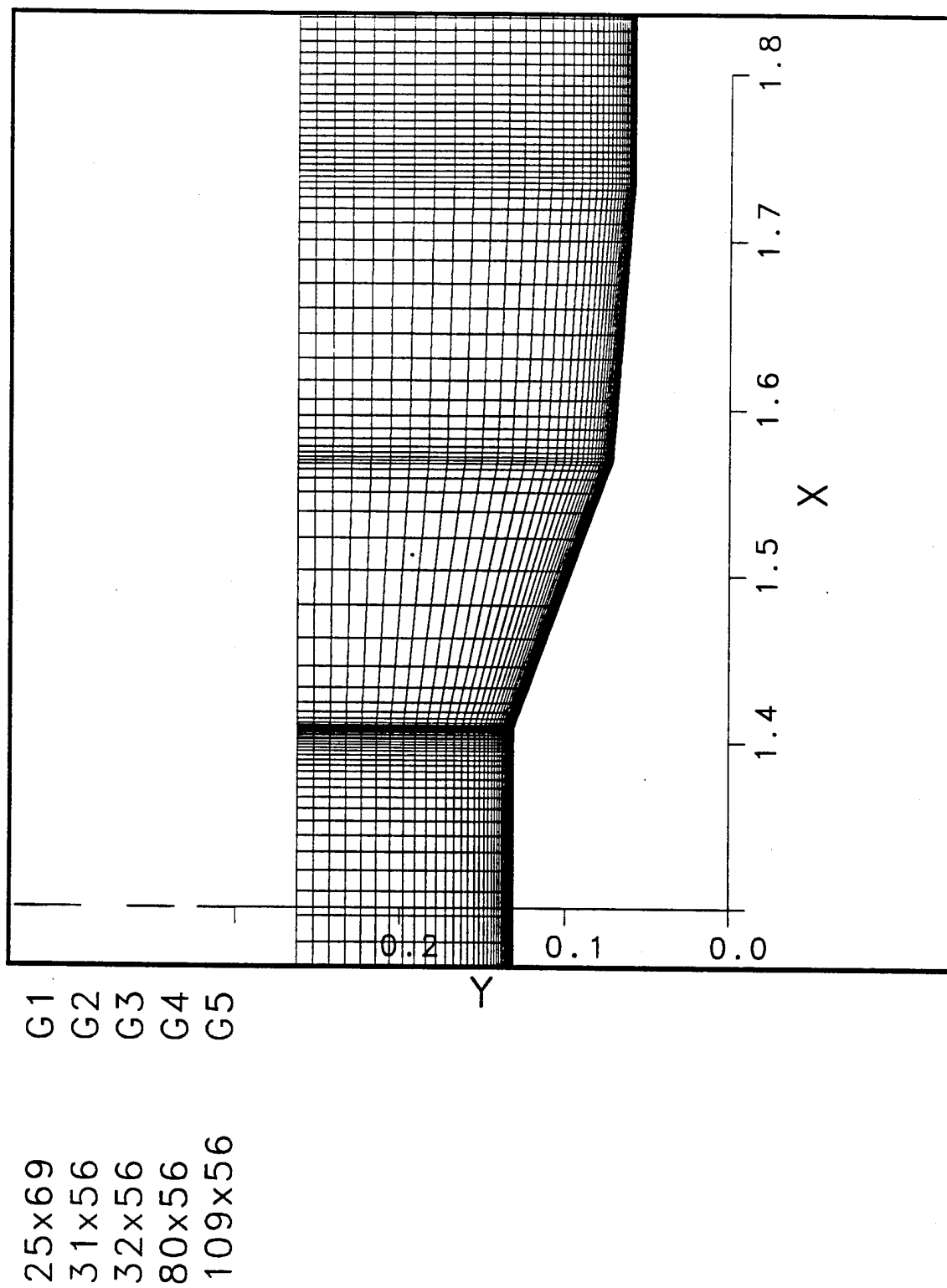
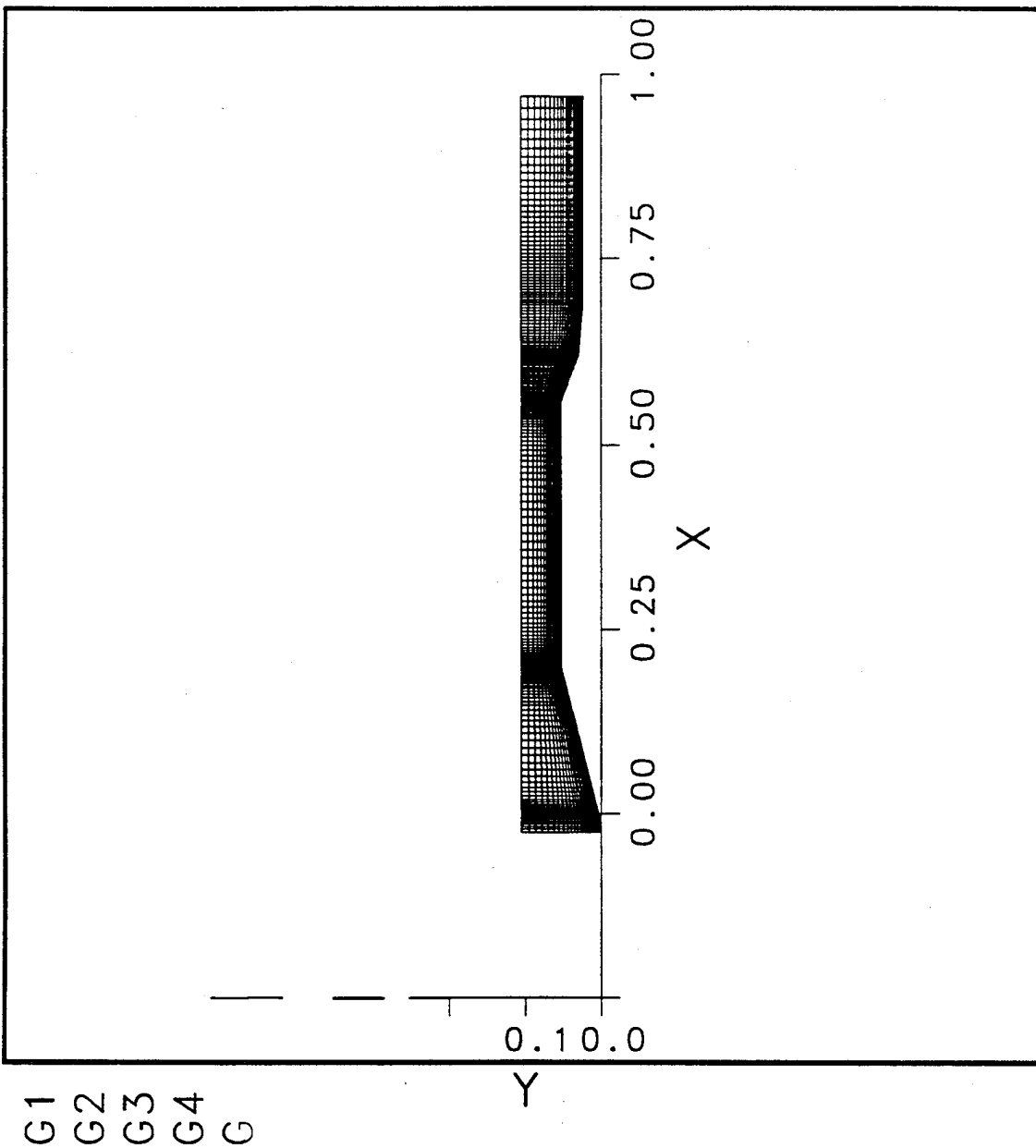


Figure 9. Details of the grid near the boattail, Configuration 2.

GRID

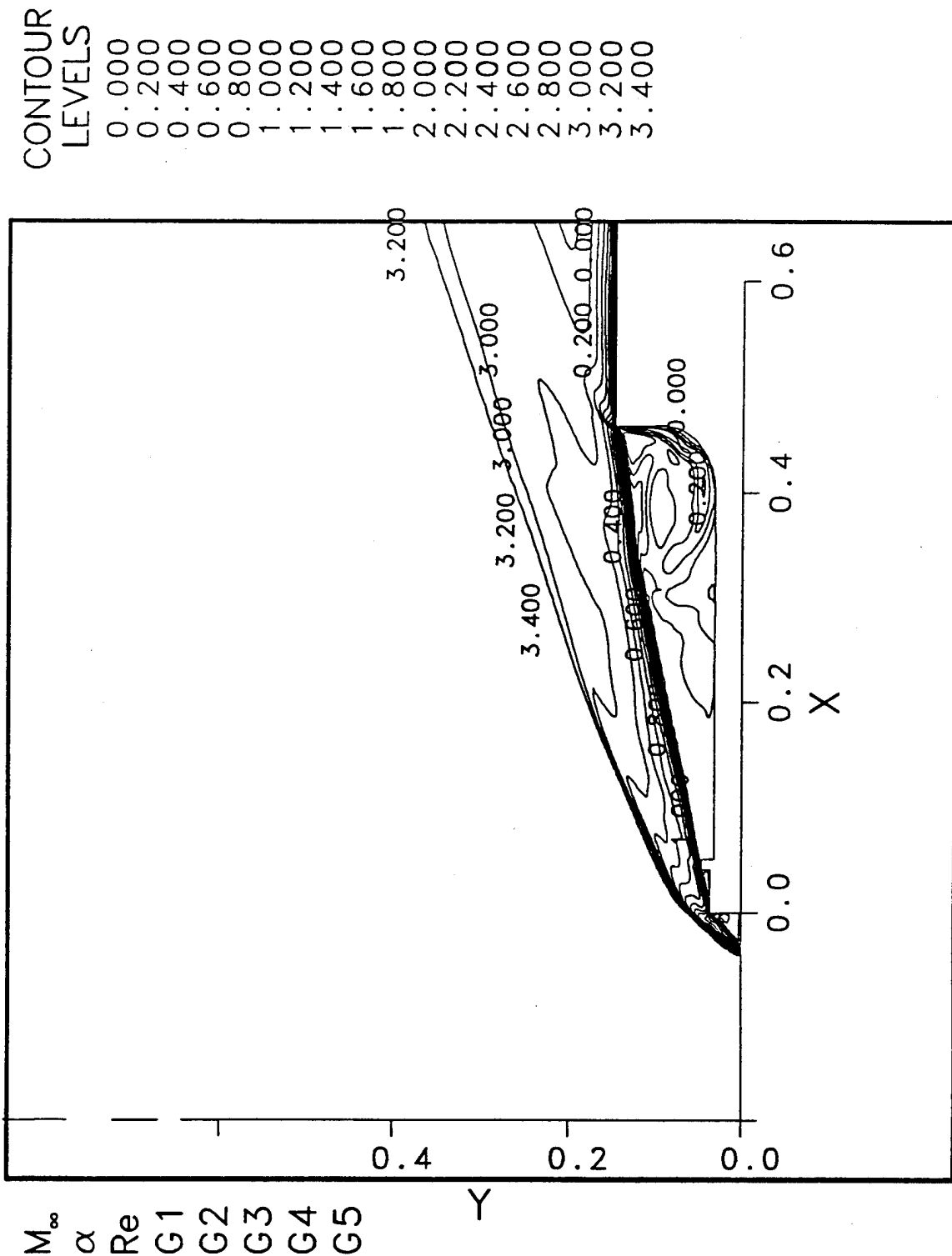


G1
G2
G3
G4
G

25x69
31x56
32x56
80x56
109x56

Figure 10. Computational grid: Configuration 3.

MACH NUMBER



3.50	M_∞
0.00°	α
1.31×10^6	Re
35x131	G1
17x114	G2
11x107	G3
105x124	G4
130x56	G5

Figure 11. Flow-field Mach contours: Configuration 1, Mach=3.5 - Flow over the spike.

MACH NUMBER

3.50
 0.00°
 1.31 * 10⁶
 35x131
 17x114
 11x107
 105x124
 130x56

M_∞
 α
 Re
 G1
 G2
 G3
 G4
 G5

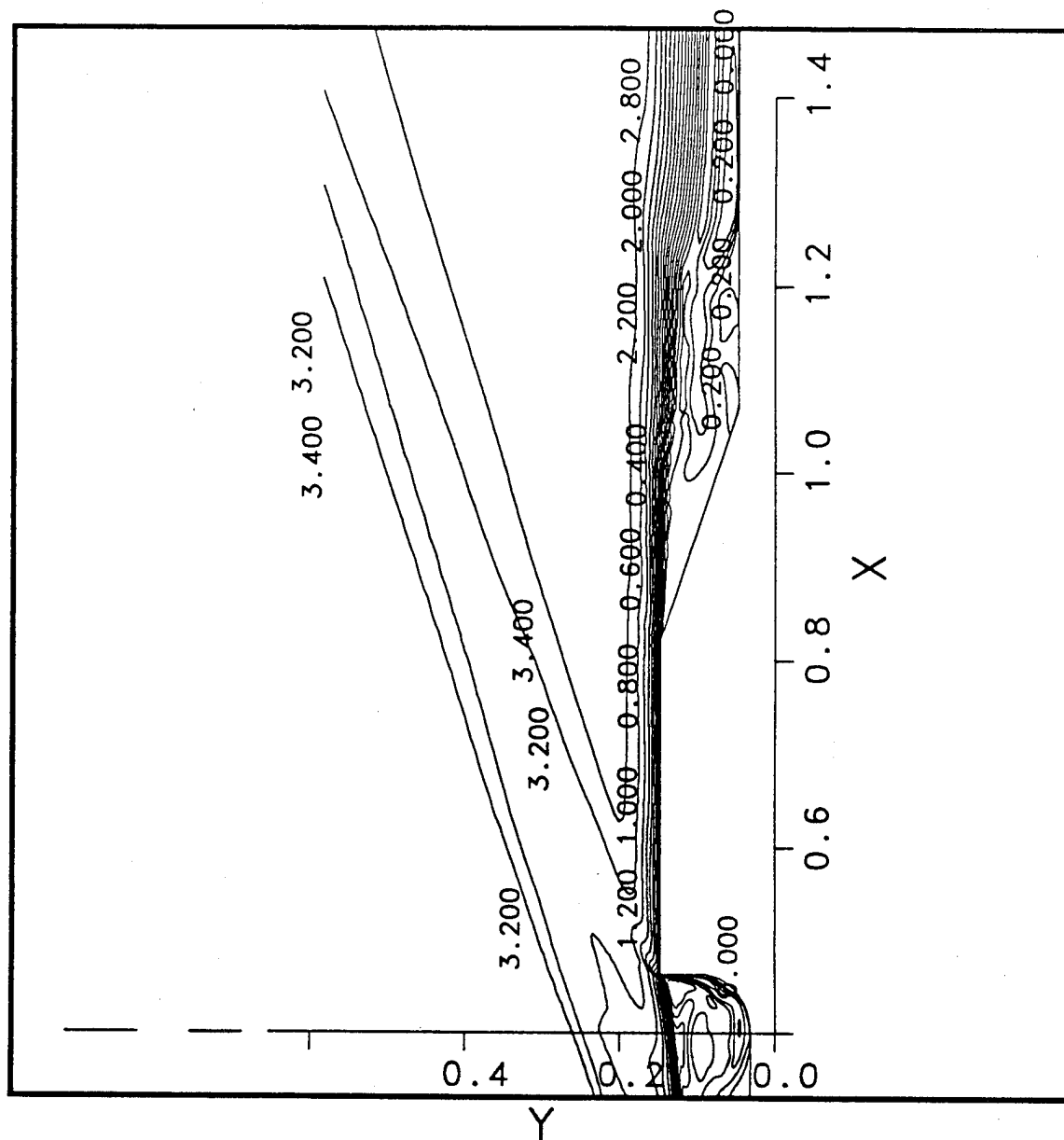


Figure 12. Flow-field Mach contours: Configuration 1, Mach=3.5 - Flow over the boattail.

MACH NUMBER

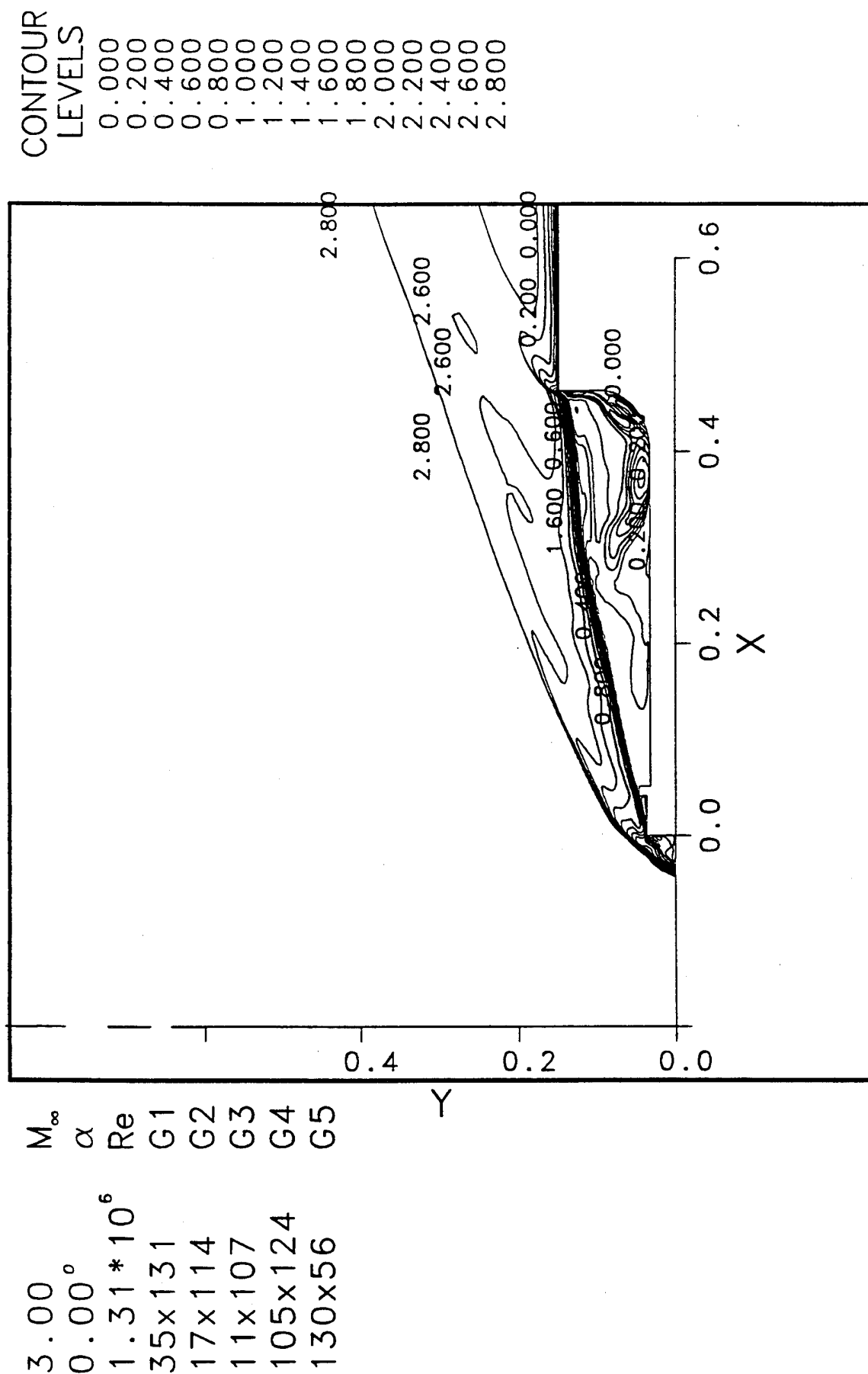


Figure 13. Flow-field Mach contours: Configuration 1, Mach=3.0 - Flow over the spike.

MACH NUMBER

3.00	M_∞
0.00°	α
1.31×10^6	Re
35x131	G1
17x114	G2
11x107	G3
105x124	G4
130x56	G5

CONTOUR
LEVELS

0.000
0.200
0.400
0.600
0.800
1.000
1.200
1.400
1.600
1.800
2.000
2.200
2.400
2.600
2.800

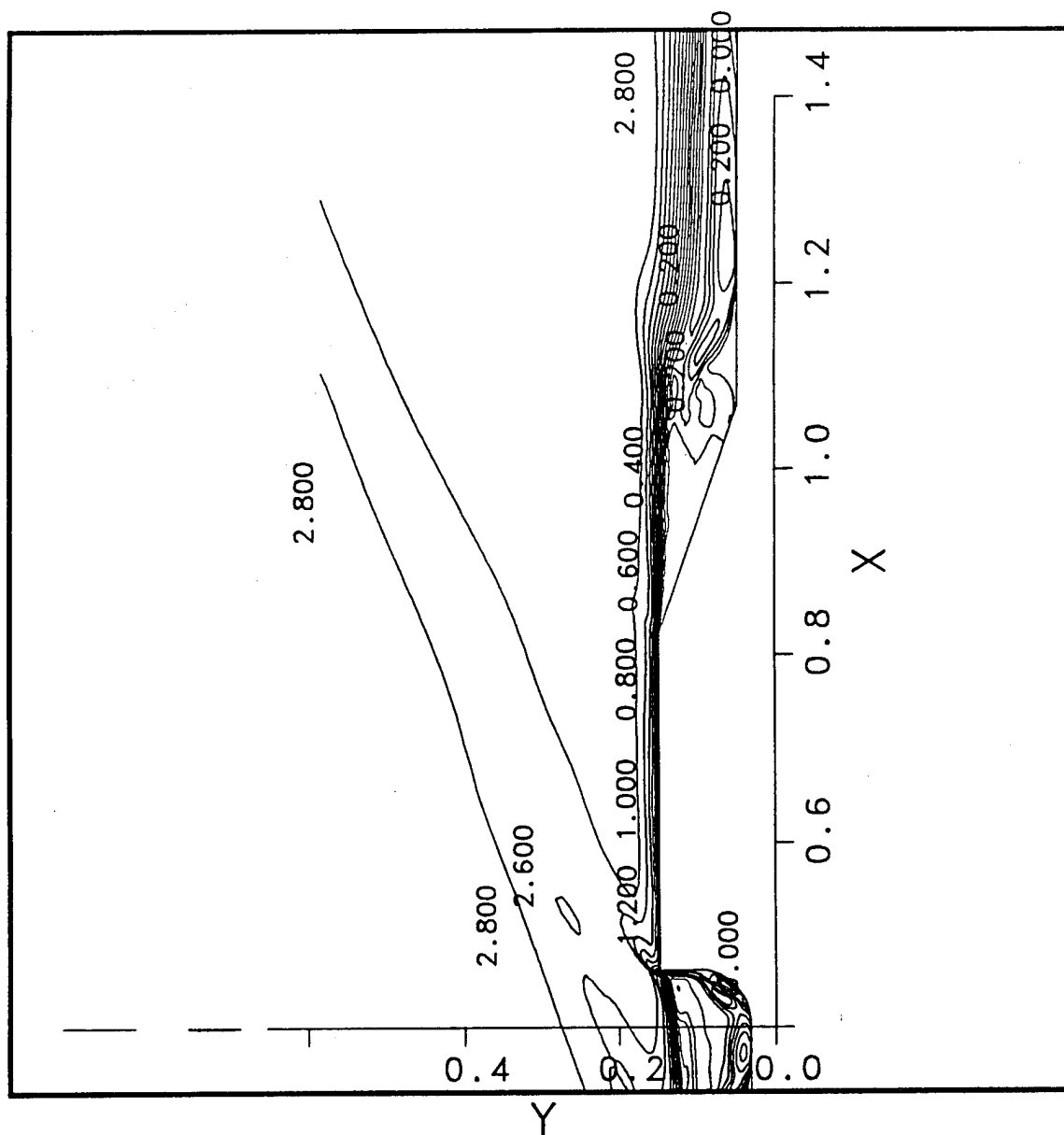


Figure 14. Flow-field Mach contours: Configuration 1, Mach=3.0 - Flow over the boattail.

MACH NUMBER

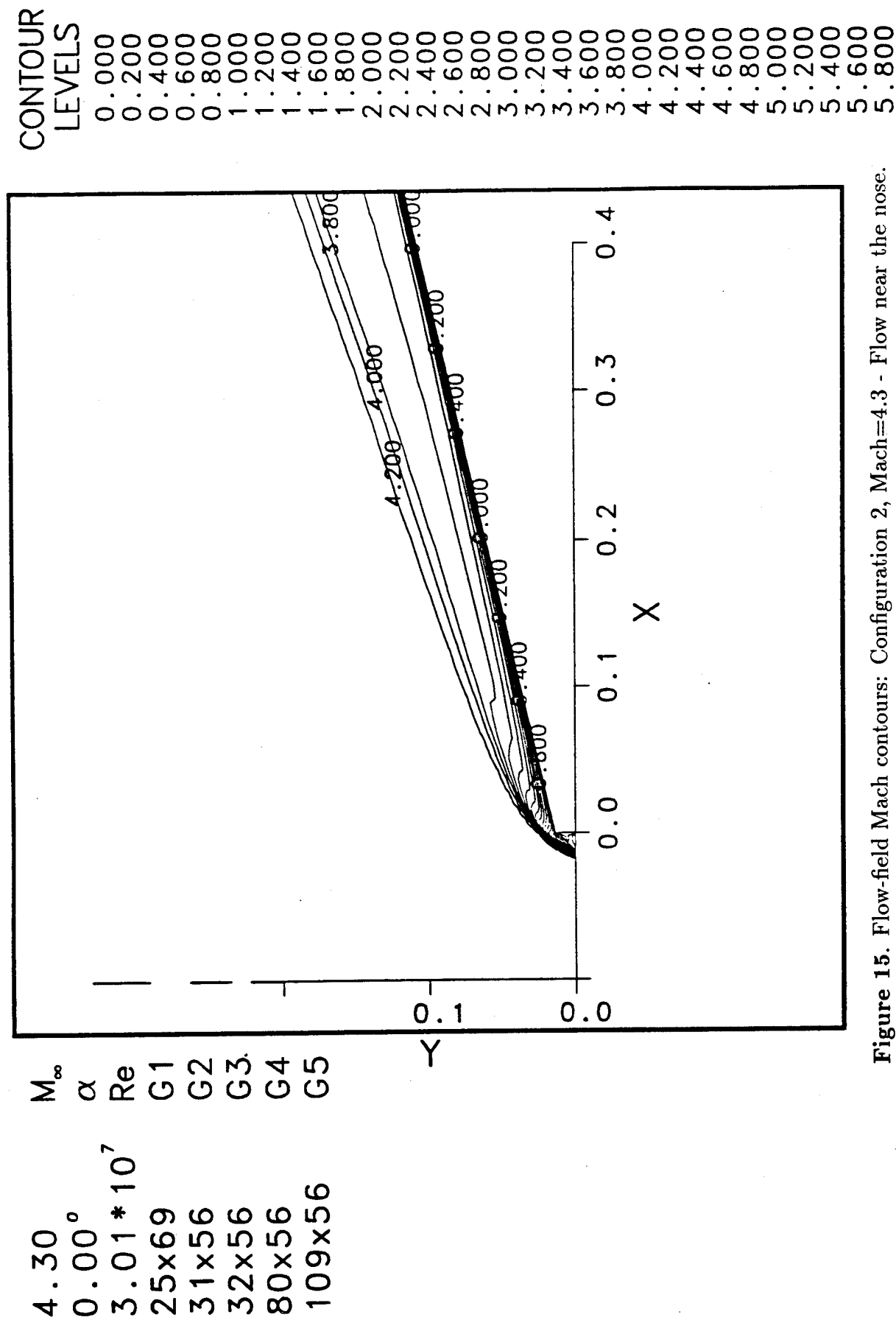


Figure 15. Flow-field Mach contours: Configuration 2, Mach=4.3 - Flow near the nose.

MACH NUMBER

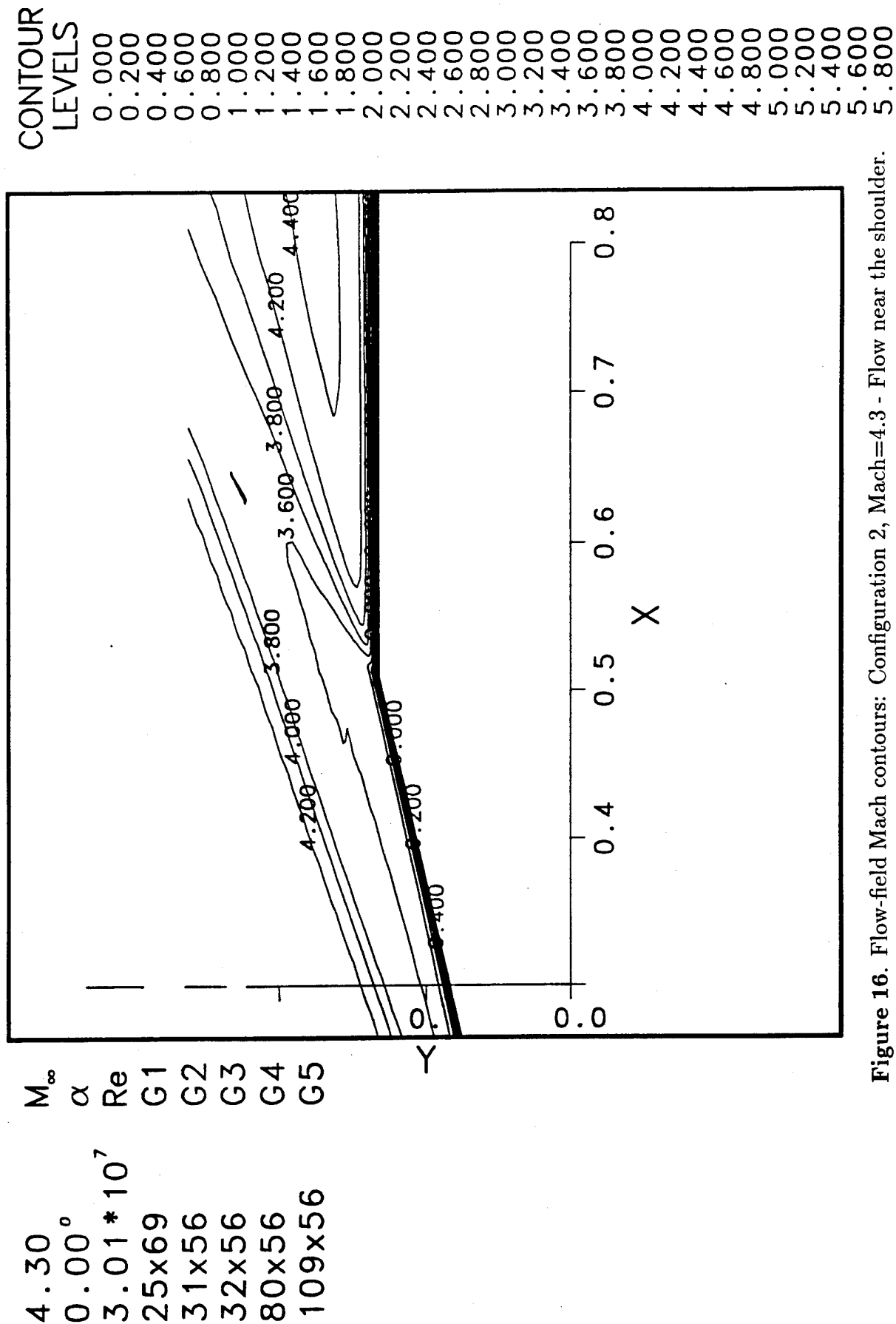


Figure 16. Flow-field Mach contours: Configuration 2, Mach=4.3 - Flow near the shoulder.

MACH NUMBER

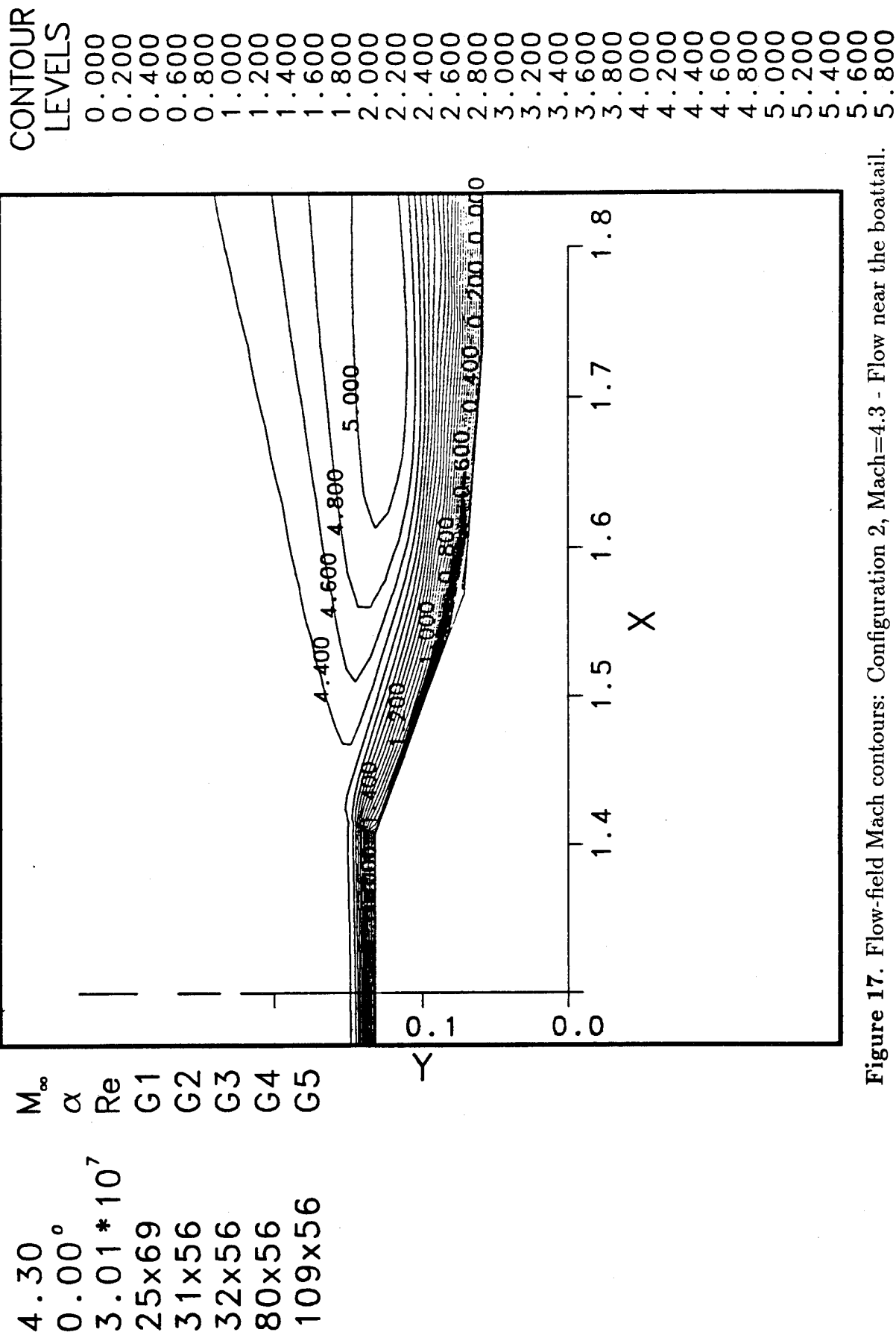


Figure 17. Flow-field Mach contours: Configuration 2, Mach=4.3 - Flow near the boattail.

MACH NUMBER

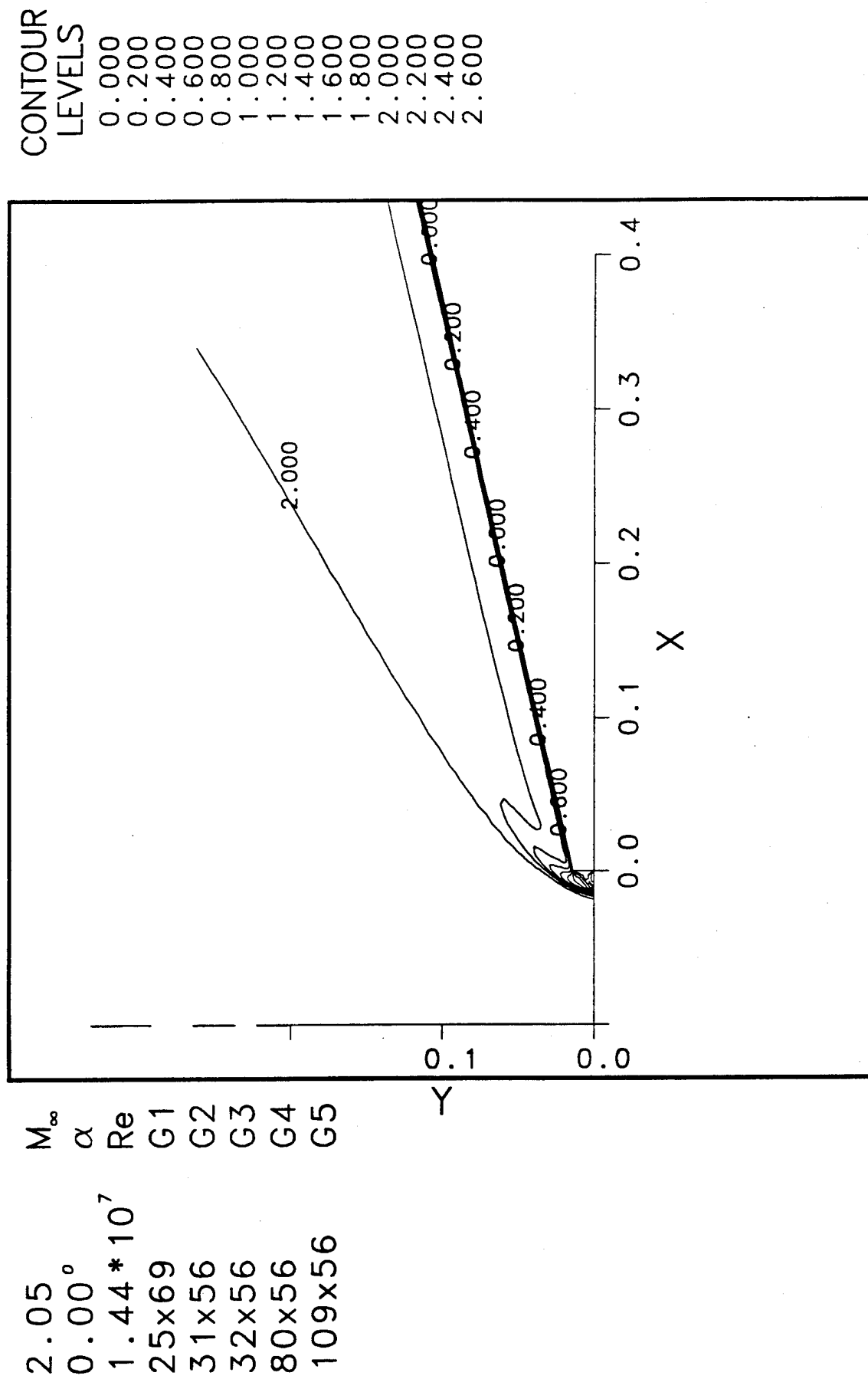


Figure 18. Flow-field Mach contours: Configuration 2, Mach=2.05 - Flow near the nose.

MACH NUMBER

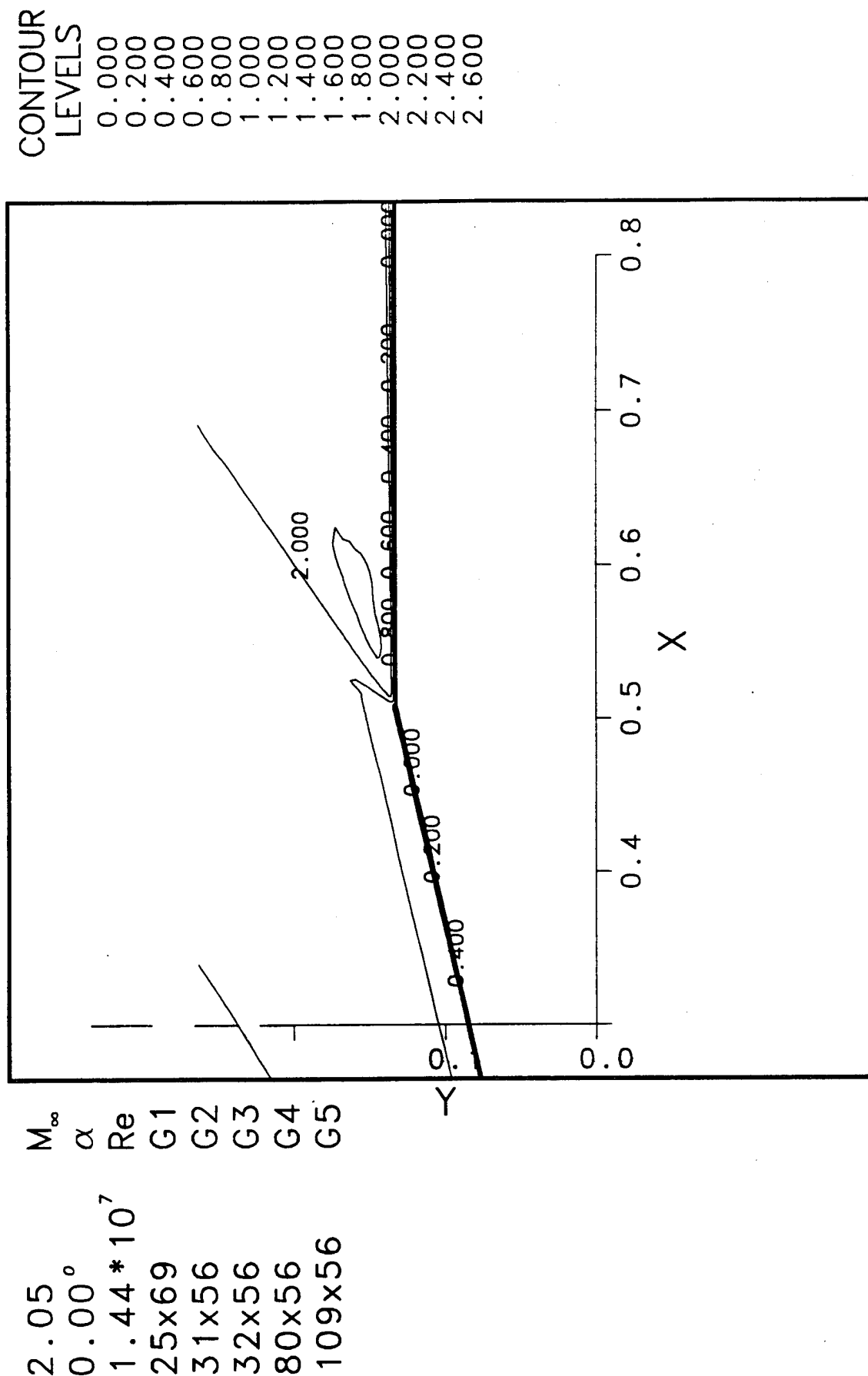


Figure 19. Flow-field Mach contours: Configuration 2, Mach=2.05 - Flow near the shoulder.

MACH NUMBER

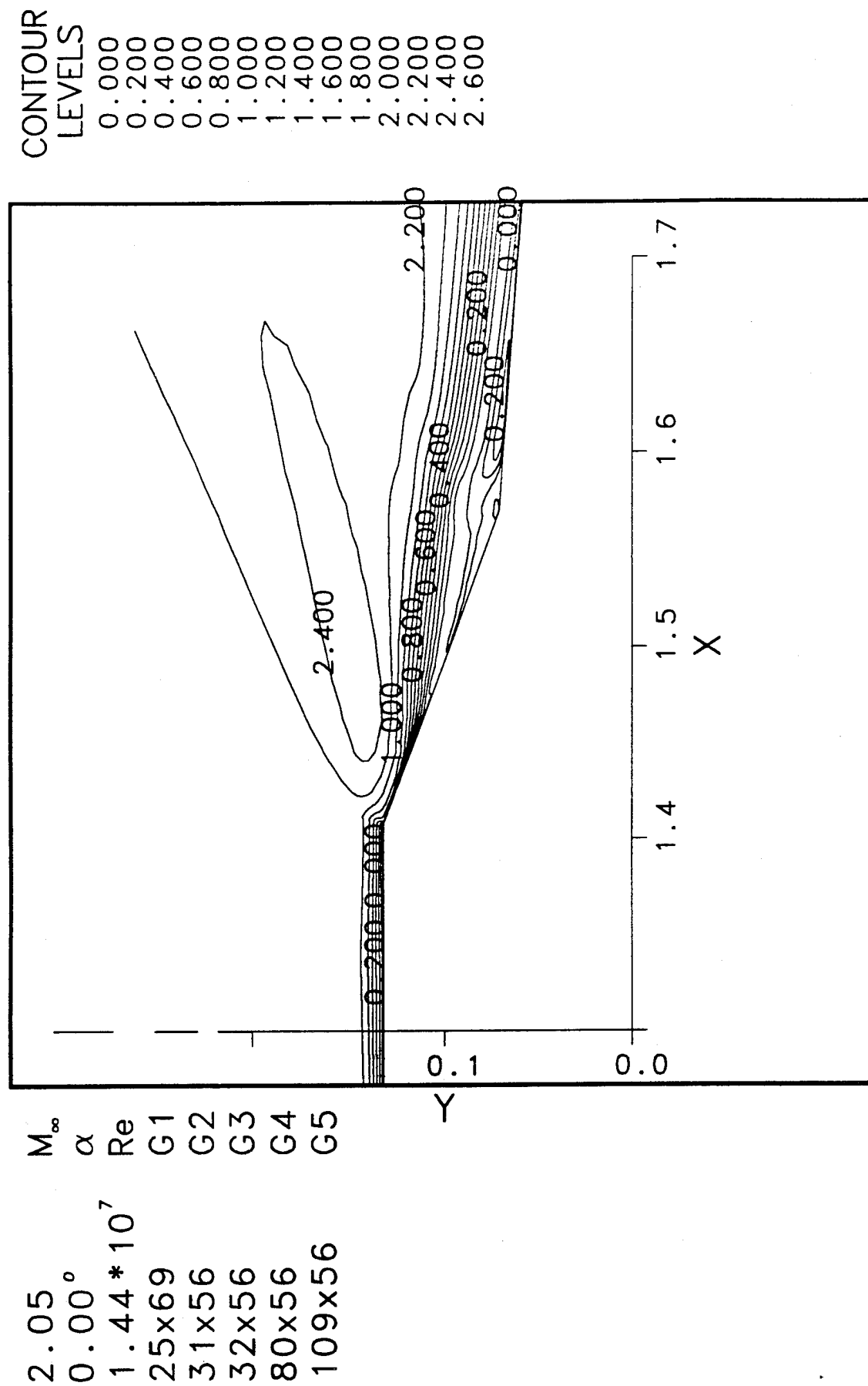


Figure 20. Flow-field Mach contours: Configuration 2, Mach=2.05 - Flow over the boattail.

2.05	M_∞
0.00°	α
1.44×10^7	Re
25x69	G1
31x56	G2
32x56	G3
80x56	G4
109x56	G5

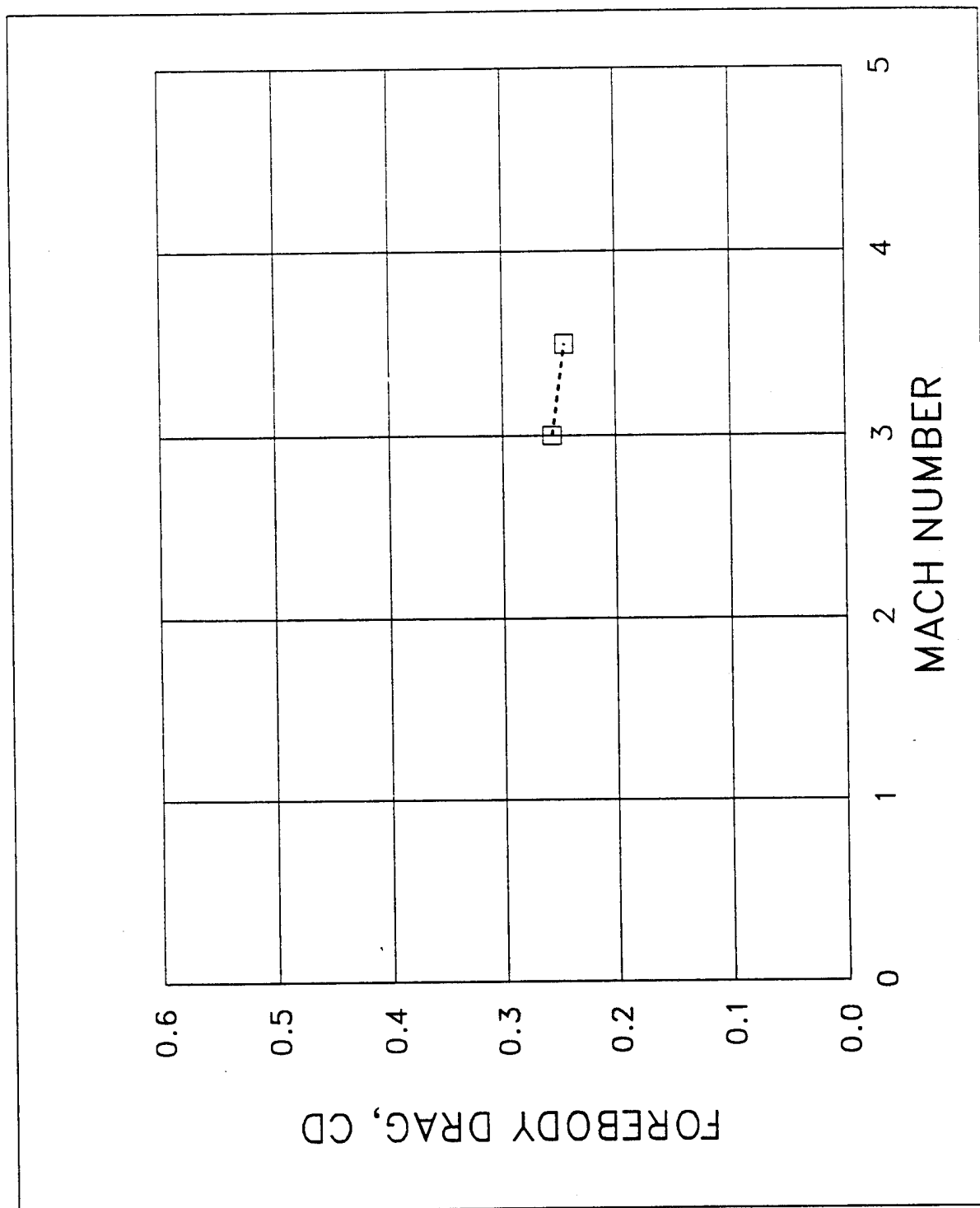


Figure 21. Total forebody drag coefficient for Config. 1.

CONFIGURATION 1 Mach 3.5

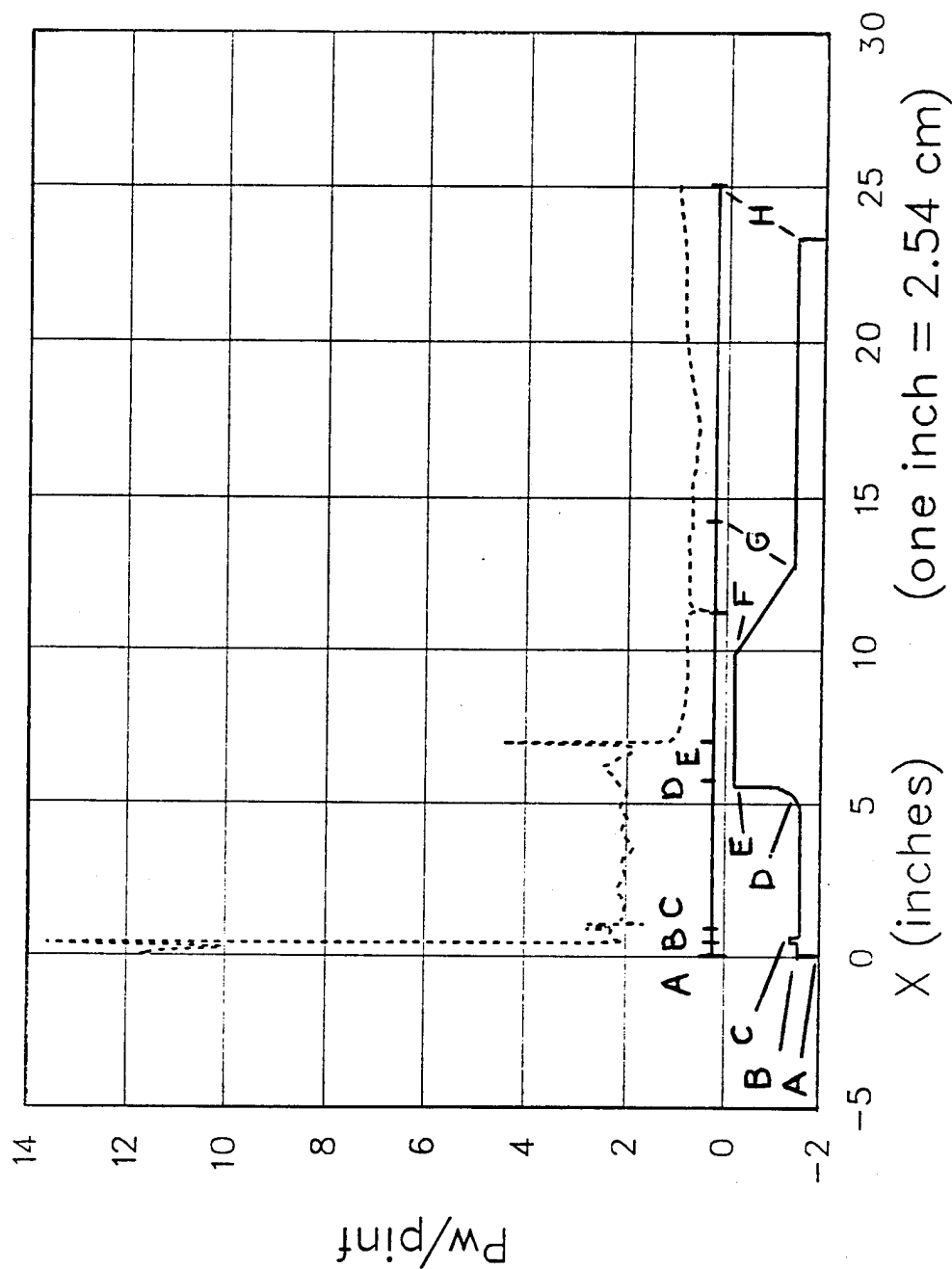


Figure 22. Surface pressure distribution for Config. 1, at $M=3.5$.

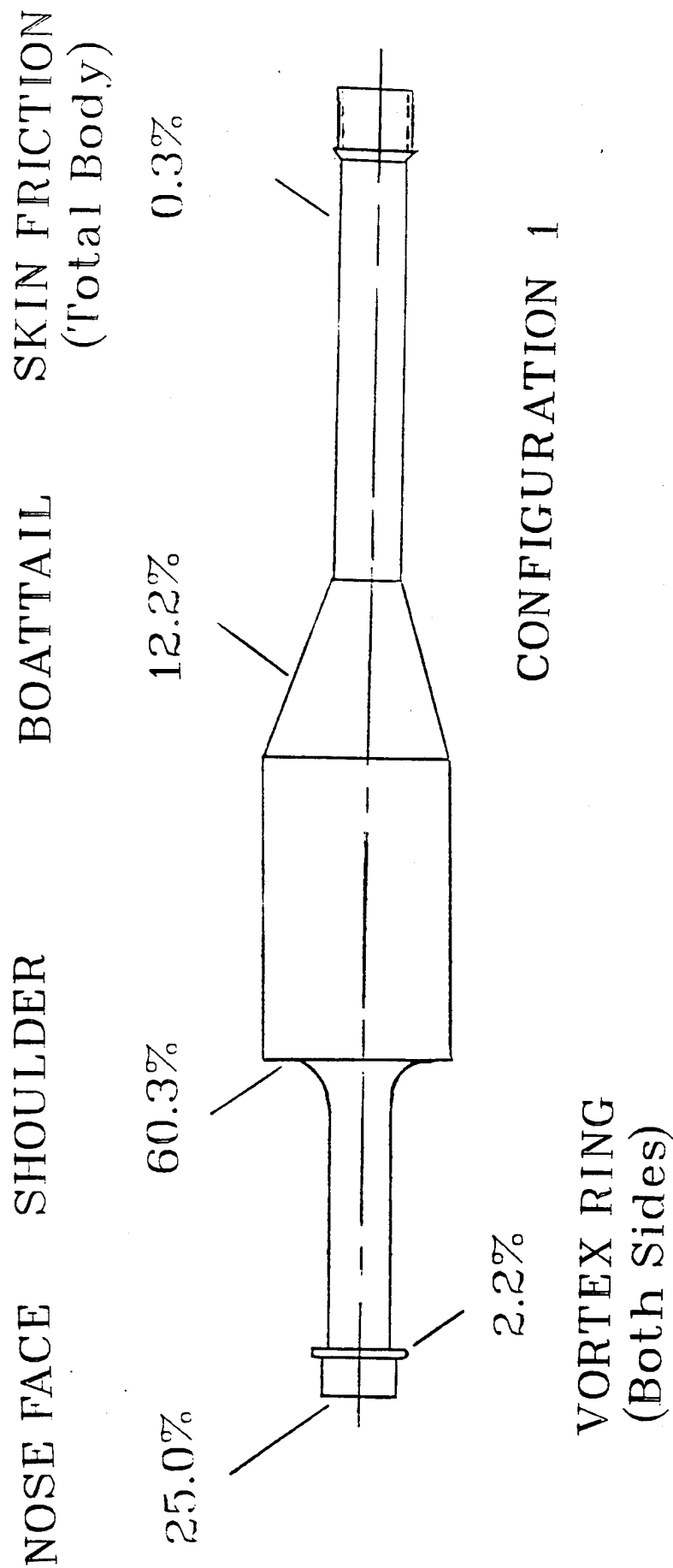


Figure 23. Drag coefficient composition for Config. 1, at $M=3.0$.

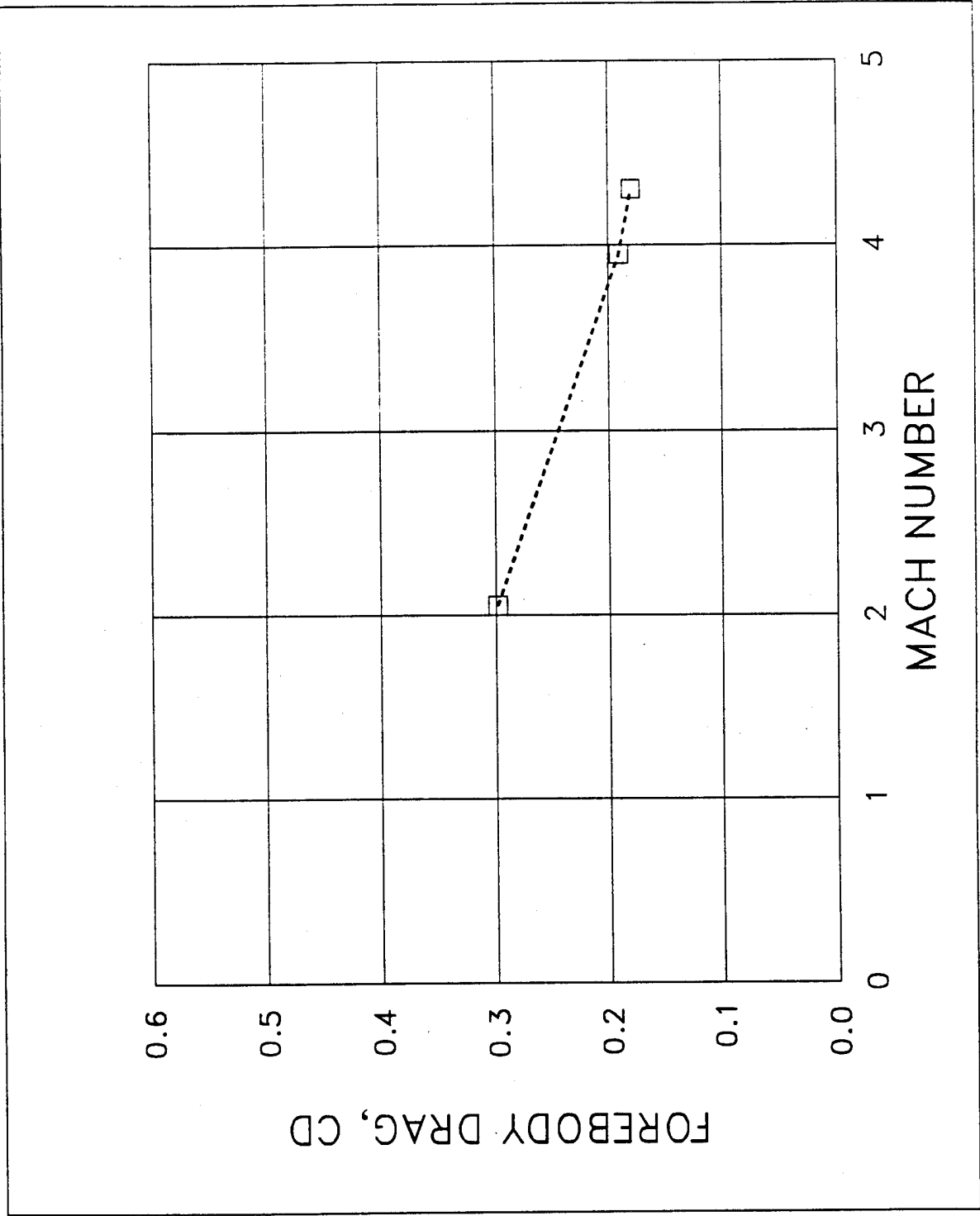


Figure 24. Total forebody drag coefficient for Config. 2.

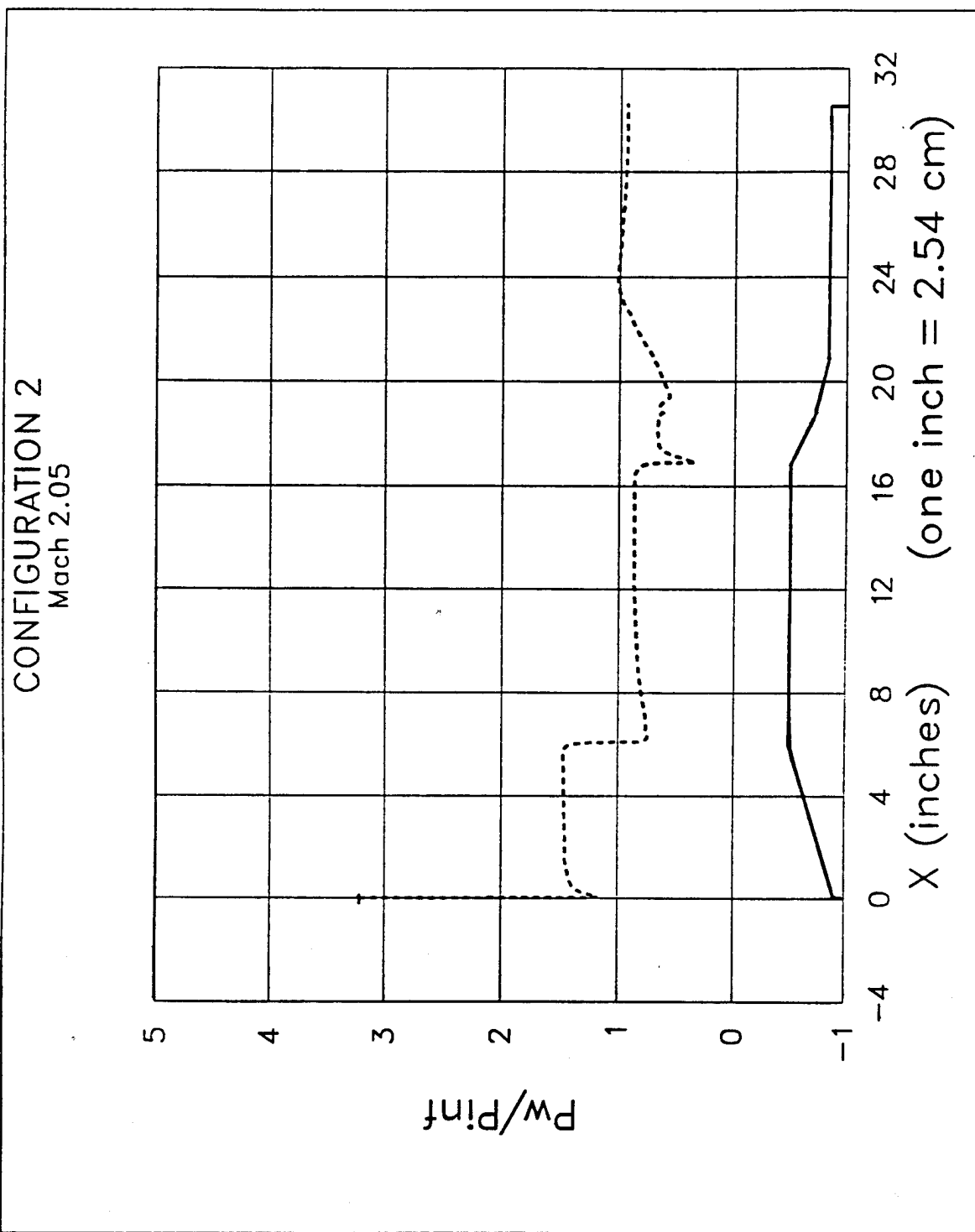


Figure 25. Surface pressure distribution for Config. 2, at $M=2.05$.

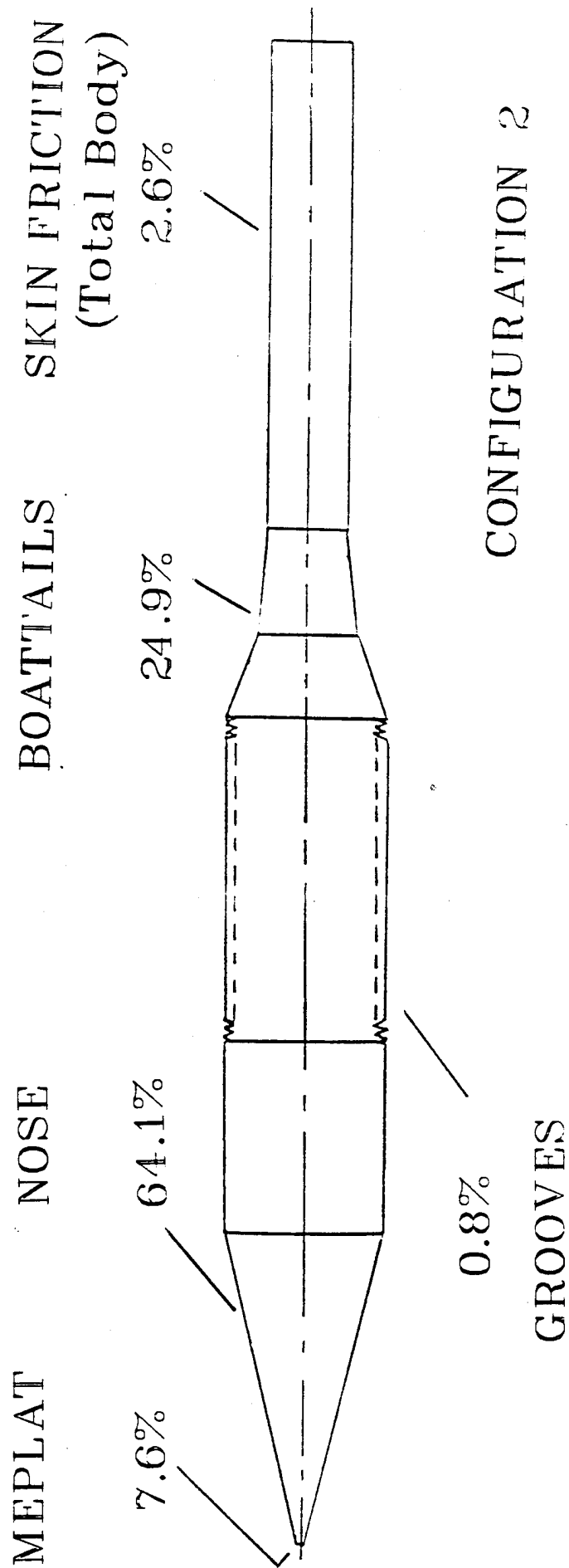


Figure 26. Drag coefficient composition for Config. 2, at $M=4.3$.

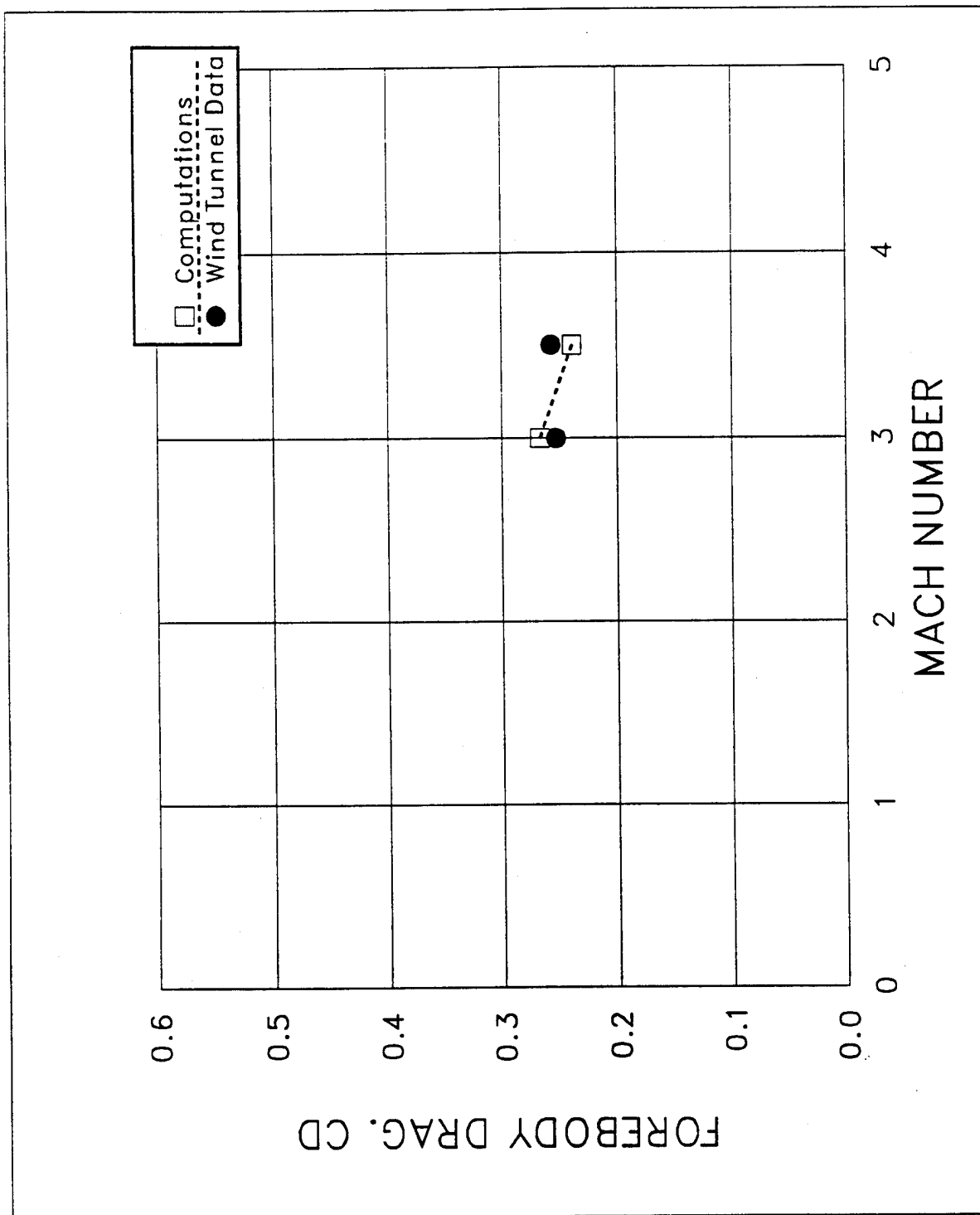


Figure 27. Total forebody drag coefficient for Config. 3.

CONFIGURATION 3
Mach 3.5

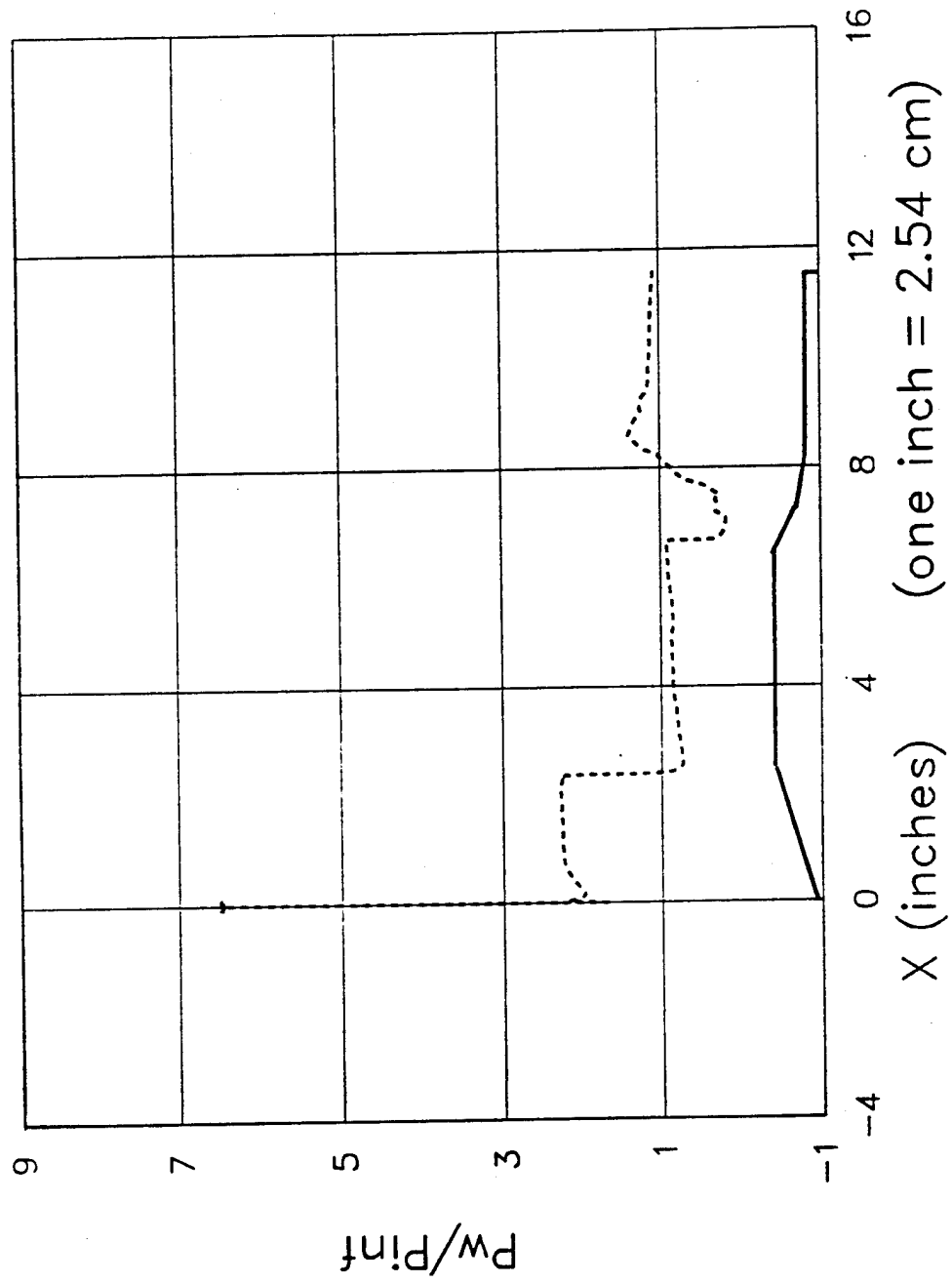
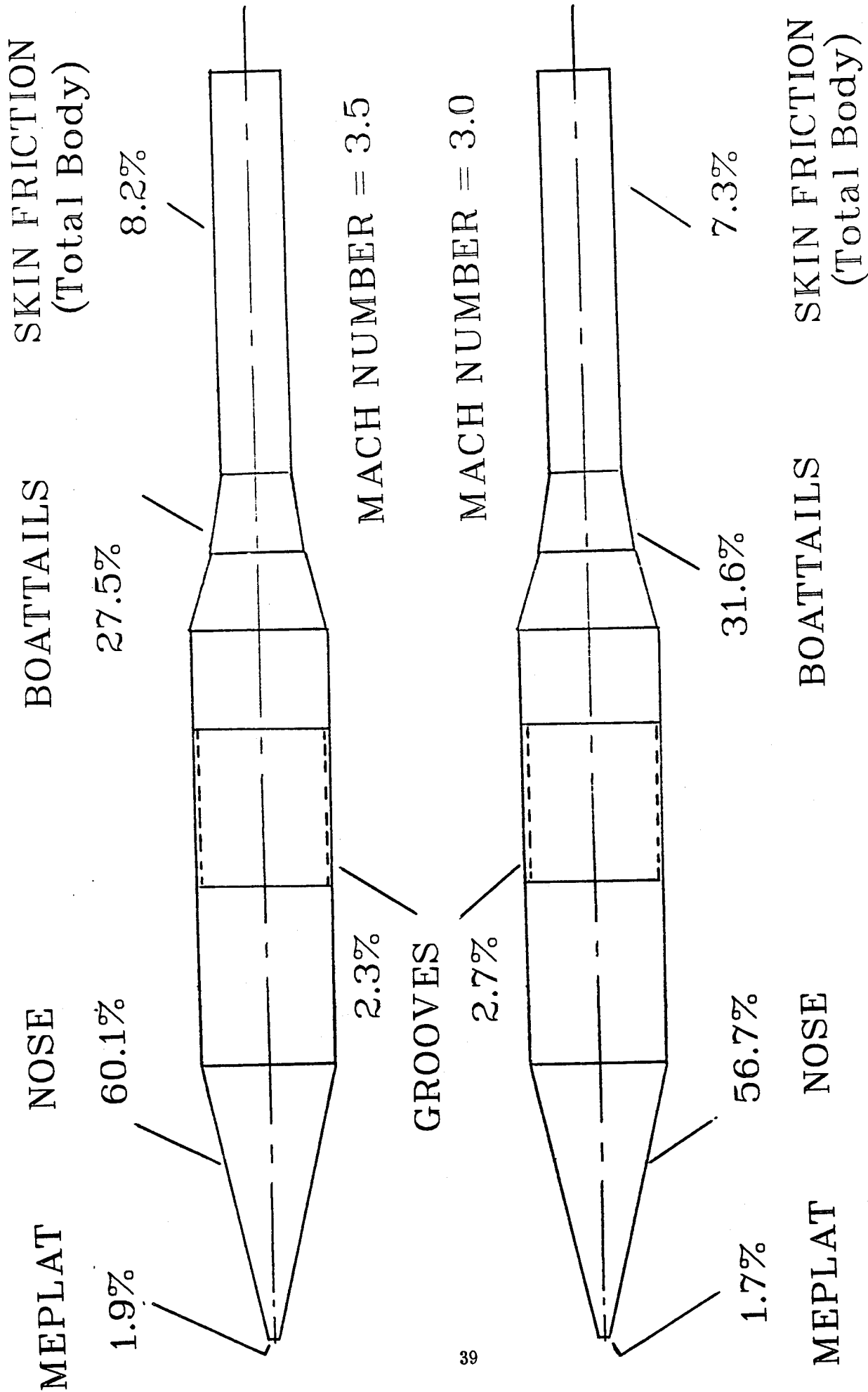


Figure 28. Surface pressure distribution for Config. 3, at $M=3.5$.



CONFIGURATION 3

Figure 29. Drag coefficient composition for Config. 3, at $M=3.5$ and 3.0 .

References

1. Mikhail, A.G., "Spiked-Nosed Projectiles: Computations and Dual Flow Modes in Supersonic Flight," J. of Spacecraft and Rockets, Vol. 28, No. 4, July-August 1991, pp. 418-424. (Also AIAA Paper 89-1820)
2. Mikhail, A.G., "Spike-Nosed Projectiles with Vortex Rings : Steady and Unsteady Flow Simulations," AIAA Paper 91-3261, September 1991.
3. Patel, N.R., and Sturek, W.B., "Multi-Tasked Numerical Simulation of Axisymmetric Ramjet Flows Using Zonal Overlapped Grids, " BRL-MR-3834, U.S. Army Ballistic Research Laboratory, Aberdeen Proving Ground, Maryland, May 1990.
4. Falkowski, E.W., "Static and Dynamic Stability Characteristics of the Supersonic Infantry Projectile at Transonic Velocities," TM-1565, U.S. Army Picatinny Arsenal, Dover, NJ, June 1965.
5. Biele, J. K., "Drag and Flow Field Characteristics of Two Complex-Shapes Projectile Type," Proceedings of the 7th International Symposium on Ballistics, held in the Hague, Netherlands, April 1983, pp. 221-229.
6. Farina, T. and Choudhary, A., "Wind Tunnel Test Results of An Advanced Multipurpose Tank Fired Projectile," ARAED-TR-91015, U.S. Army Armament Research, Development and Engineering Center, Picatinny Arsenal, NJ, October 1991.
7. Baldwin, B.S. and Lomax, H., "Thin-Layer Approximation and Algebraic Model for Separated Turbulent Flows," AIAA Paper 78-257, January 1978.
8. Danberg, J.E. and Patel, N.R., "An Algebraic Turbulent Model For Flow Separation Caused by Forward Facing Steps," BRL-MR-3791, U.S. Army Ballistic Research Laboratory, Aberdeen Proving Ground, Maryland, December 1989.
9. Haupt, B. F., Buff, R.S. and Koenig, K., "Aerodynamic Effects of Probe-Induced Flow Separation on Bluff Bodies at Transonic Mach Numbers," AIAA Paper 85-0103, January 1985.
10. Calarese, W. and Hankey, W.L., " Modes of Shock Wave Oscillations on Spike-Tipped Bodies," AIAA Journal, Vol. 23, No. 2, February 1985, pp. 185-192.
11. Shang, J.S., Hankey, W.L. and Smith, R.E., "Flow Oscillations of Spike-Tipped Bodies," AIAA Journal, Vol. 20, No. 1, January 1982, pp. 25-26.
12. Mikhail, A. G., "Data Correlation and Surface Groove Drag for Kinetic Energy Projectiles," J. of Spacecraft and Rockets, Vol. 26, No. 5, Sept.-Oct. 1989, pp. 308-313. (Also AIAA Paper 88-2541)

LIST OF SYMBOLS

A_{ref}	= reference area, $(\pi d^2/4)$
C_D	= drag coefficient, drag force/ $(0.5\rho V^2 A_{ref})$
C_p	= specific heat under constant pressure
C_v	= specific heat under constant volume
d	= projectile reference diameter
e	= specific total energy
J	= Jacobian of the coordinate transformation
M	= Mach number
p	= static pressure
Re	= Reynolds number per unit length
Rel	= Reynolds number, based on reference diameter
T	= static temperature
u, v	= velocity components in the x, y directions
V_∞	= free stream flow velocity
x, y	= Cartesian coordinates for 2-D case, also axial and radial coordinates for axisymmetric case

Greek Symbols

α	= angle of attack
γ	= ratio of specific heats
ρ	= density
μ	= laminar (molecular) viscosity coefficient
ϵ	= turbulent eddy viscosity coefficient
ξ, η	= transformed coordinates in the computational plane for the coordinates x, y

Subscripts

o	= denotes total (stagnation) condition
∞	= free stream condition
w	= location on the body surface (wall)

INTENTIONALLY LEFT BLANK.

<u>NO. OF COPIES</u>	<u>ORGANIZATION</u>
2	DEFENSE TECHNICAL INFO CTR ATTN DTIC DDA 8725 JOHN J KINGMAN RD STE 0944 FT BELVOIR VA 22060-6218

1	DIRECTOR US ARMY RESEARCH LAB ATTN AMSRL OP SD TA 2800 POWDER MILL RD ADELPHI MD 20783-1145
---	---

3	DIRECTOR US ARMY RESEARCH LAB ATTN AMSRL OP SD TL 2800 POWDER MILL RD ADELPHI MD 20783-1145
---	---

1	DIRECTOR US ARMY RESEARCH LAB ATTN AMSRL OP SD TP 2800 POWDER MILL RD ADELPHI MD 20783-1145
---	---

ABERDEEN PROVING GROUND

5	DIR USARL ATTN AMSRL OP AP L (305)
---	---------------------------------------

<u>NO. OF COPIES</u>	<u>ORGANIZATION</u>
11	<p>COMMANDER US ARMY ARDEC ATTN AMSTA AR AET A C NG J GRAU S KAHN H HUDGINS M AMORUSO E BROWN B WONG W TOLEDO S CHUNG C LIVECCHIA G MALEJKO PICATINNY ARSENAL NJ 07806-5000</p>
3	<p>COMMANDER US ARMY ARDEC ATTN AMSTA AR CCH B B KONRAD E FENNELL T LOUZEIRO PICATINNY ARSENAL NJ 07806-5000</p>
4	<p>COMMANDER US ARMY ARDEC ATTN AMSTA AR FSE A GRAF D LADD E ANDRICPOULIS K CHEUNG PICATINNY ARSENAL NJ 07806-5000</p>
6	<p>COMMANDER US ARMY ARDEC ATTN AMSTA AR CCL D F PUZYCKI D CONWAY D DAVIS K HAYES M PINCAY W SCHUPP PICATINNY ARSENAL NJ 07806-5000</p>
1	<p>PROJECT MANAGER TANK MAIN ARMAMENT SYSTEM ATTN SFAE ASM TMA MAJ B HELD R KOWALSKI PICATINNY ARSENAL NJ 07806-5000</p>

<u>NO. OF COPIES</u>	<u>ORGANIZATION</u>
3	<p>US ARMY RESEARCH OFFICE ATTN G ANDERSON K CLARK T DOLIGOWSKI RESEARCH TRIANGLE PARK NC 27709-2211</p>
2	<p>COMMANDER US ARMY RESEARCH LABORATORY ATTN AMSRL MA CA M FLETCHER M O'DAY 405 ARSENAL ST WATERTOWN MA 02172-0001</p>
2	<p>DIRECTOR BENET LABS ATTN AMSTA AR CCB T S SOPOK P ALTO WATERVLIET NY 12189</p>
3	<p>COMMANDER US NAVAL SURFACE WARFARE CTR ATTN CODE DK20 CLARE MOORE DEVAN DAHLGREN VA 22448-5000</p>
2	<p>COMMANDER US NAVAL SURFACE WARFARE CTR APPLIED MATHEMATICS BRANCH ATTN CODE R44 A WARDLAW F PRIOLO SILVER SPRING MD 20903-5000</p>
1	<p>DIRECTOR NASA AMES RESEARCH CTR ATTN MS 258 1 L SCHIFF MOFFETT FIELD CA 94035</p>
2	<p>DIRECTOR SANDIA NATIONAL LABS ATTN DIVISION 1636 W OBJERKAMPF W WOLFE PO BOX 5800 ALBUQUERQUE NM 87185</p>

<u>NO. OF</u> <u>COPIES</u>	<u>ORGANIZATION</u>
1	COMMANDER US ARMY MISSILE COMMAND ATTN AMSMI RD SS AT W WALKER REDSTONE ARSENAL AL 35898-5010
2	NASA LANGLEY RESEARCH CTR ATTN TECH LIBRARY M HEMSCH LANGLEY STATION HAMPTON VA 23665
3	AIR FORCE ARMAMENT LAB ATTN AFATL FXA B SIMPON G ABATE R ADELGREN EGLIN AFB FL 32542-5434
1	DIRECTOR LOS ALAMOS NATIONAL LAB ATTN MS G770 W HOGAN LOS ALAMOS NM 87545
1	DIRECTOR ARPA ATTN TACTICAL TECHNOLOGY OFC 3701 N FAIRFAX DR ARLINGTON VA 22203-1714
2	US MILITARY ACADEMY DEPT OF CIVIL & MCHNCL ENGRNG ATTN M COSTELLO A DULL WEST POINT NY 10996

<u>NO. OF</u> <u>COPIES</u>	<u>ORGANIZATION</u>
	<u>ABERDEEN PROVING GROUND</u>
22	DIR, USARL ATTN: AMSRL-WT, I. MAY AMSRL-WT-P, A. HORST AMSRL-WT-PA, T. MINOR AMSRL-WT-PB, E. SCHMIDT A. MIKHAIL (5 CP) P. PLOSTINS V. OSKAY J. GARNER J. SAHU B. GUIDOS D. SAVICK H. EDGE M. BUNDY K. FANSLER G. COOPER K. SOENCKSEN A. ZIELINSKI AMSRL-WT-PD, B. BURNS
2	CDR, USAATC ATTN: STECS-EN-PM, J. FALLER D. HORTON
2	CDR, USAARDEC ATTN: AMSTA-AR-FSF-T, R. LIESKE F. MIRABELLE

INTENTIONALLY LEFT BLANK.

USER EVALUATION SHEET/CHANGE OF ADDRESS

This Laboratory undertakes a continuing effort to improve the quality of the reports it publishes. Your comments/answers to the items/questions below will aid us in our efforts.

1. ARL Report Number ARL-TR-893 Date of Report November 1995

2. Date Report Received _____

3. Does this report satisfy a need? (Comment on purpose, related project, or other area of interest for which the report will be used.) _____

4. Specifically, how is the report being used? (Information source, design data, procedure, source of ideas, etc.) _____

5. Has the information in this report led to any quantitative savings as far as man-hours or dollars saved, operating costs avoided, or efficiencies achieved, etc? If so, please elaborate. _____

6. General Comments. What do you think should be changed to improve future reports? (Indicate changes to organization, technical content, format, etc.) _____

CURRENT ADDRESS

Organization

Name

Street or P.O. Box No.

City, State, Zip Code

7. If indicating a Change of Address or Address Correction, please provide the Current or Correct address above and the Old or Incorrect address below.

OLD ADDRESS

Organization

Name

Street or P.O. Box No.

City, State, Zip Code

(Remove this sheet, fold as indicated, tape closed, and mail.)
(DO NOT STAPLE)